Final Technical Report

Recovery Act: Strategies for Voltage Control and Transient Stability Assessment

Ian A. Hiskens

DOE Award Number: DE-EE0001382
Project Period: November 1, 2009 to October 31, 2012

Principal Investigator:
Professor Ian Hiskens
Phone: (734) 615-7076
Email: hiskens@umich.edu

Recipient Organization:
University of Michigan
Ann Arbor, MI 48109

Other Team Organizations:
Detroit Edison Company - DTE Energy
One Energy Plaza
Detroit, MI 48066

Report Date: September 25, 2013

Acknowledgment: This report is based upon work supported by the U.S. Department of Energy under Award No. DE-EE0001382.
Disclaimer: Any findings, opinions, and conclusions or recommendations expressed in this report are those of the author(s) and do not necessarily reflect the views of the Department of Energy.
Proprietary Data Notice: The report does not contain any patentable material or protected data.

Contents

1 Executive Summary

As wind generation grows, its influence on power system performance will becoming increasingly noticeable. Wind generation differs from traditional forms of generation in numerous ways though, motivating the need to reconsider the usual approaches to power system assessment and performance enhancement. The project has investigated the impact of wind generation on transient stability and voltage control, identifying and addressing issues at three distinct levels of the power system: 1) at the device level, the physical characteristics of wind turbine generators (WTGs) are quite unlike those of synchronous machines, 2) at the wind-farm level, the provision of reactive support is achieved through coordination of numerous dissimilar devices, rather than straightforward generator control, and 3) from a systems perspective, the location of wind-farms on the sub-transmission network, coupled with the variability inherent in their power output, can cause complex voltage control issues.

The project has sought to develop a thorough understanding of the dynamic behaviour of type-3 WTGs, and in particular the WECC generic model. The behaviour of such models is governed by interactions between the continuous dynamics of state variables and discrete events associated with limits. It was shown that these interactions can be quite complex, and may lead to switching deadlock that prevents continuation of the trajectory. Switching hysteresis was proposed for eliminating deadlock situations. Various type-3 WTG models include control blocks that duplicate integrators. It was shown that this leads to non-uniqueness in the conditions governing steady-state, and may result in pre- and post-disturbance equilibria not coinciding. It also gives rise to a zero eigenvalue in the linearized WTG model. In order to eliminate the anomalous behaviour revealed through this investigation, WECC has now released a new generic model for type-3 WTGs.

Wind-farms typically incorporate a variety of voltage control equipment including tap-changing transformers, switched capacitors, SVCs, STATCOMs and the WTGs themselves. The project has considered the coordinated control of this equipment, and has addressed a range of issues that arise in wind-farm operation. The first concerns the ability of WTGs to meet reactive power requirements when voltage saturation in the collector network restricts the reactive power availability of individual generators. Secondly, dynamic interactions between voltage regulating devices have been investigated. It was found that under certain realistic conditions, tap-changing transformers may exhibit instability. In order to meet cost, maintenance, fault tolerance and other requirements, it is desirable for voltage control equipment to be treated as an integrated system rather than as independent devices. The resulting high-level scheduling of wind-farm reactive support has been investigated. In addressing this control problem, several forms of future information were considered, including exact future knowledge and stochastic predictions. Deterministic and Stochastic Dynamic Programming techniques were used in the development of control algorithms. The results demonstrated that while exact future knowledge is very useful, simple prediction methods yield little benefit.

The integration of inherently variable wind generation into weak grids, particularly sub-transmission networks that are characterized by low X/R ratios, affects bus voltages, regulating devices and line flows. The meshed structure of these networks adds to the complexity, especially when wind generation is distributed across multiple nodes. A range of techniques have been considered for analyzing the impact of wind variability on weak grids. Sensitivity analysis, based on the power-flow Jacobian, was used to highlight sections of a system that are most severely affected by wind-power variations. A continuation power flow was used to determine parameter changes that reduce the impact of wind-power variability. It

was also used to explore interactions between multiple wind-farms. Furthermore, these tools have been used to examine the impact of wind injection on transformer tap operation in sub-transmission networks. The results of a tap operation simulation study show that voltage regulation at wind injection nodes increases tap change operations. The tradeoff between local voltage regulation and tap change frequency is fundamentally important in optimizing the size of reactive compensation used for voltage regulation at wind injection nodes. Line congestion arising as a consequence of variable patterns of wind-power production has also been investigated. Two optimization problems have been formulated, based respectively on the DC and AC power flow models, for identifying vulnerable line segments. The DC optimization is computationally more efficient, whereas the AC sensitivity-based optimization provides greater accuracy.

2 Dynamics of Type-3 Wind Turbine Generator Models

2.1 Introduction

The dynamic behaviour of wind turbine generators (WTGs) is quite different to that of synchronous generators. It is to be expected, therefore, that the dynamic performance of power systems may change as traditional generation is displaced by ever increasing numbers of WTGs. Numerous studies have investigated this issue, and have drawn various conclusions [1, 2, 3, 4, 5]. This chapter does not address the system-wide dynamic implications of large-scale wind generation *per se*. Rather, it focuses on the dynamic modelling of WTGs. In particular, the modelling of type-3 WTGs is considered, as they are currently the dominant technology for new wind-farm developments. Such WTGs are also known as doubly fed induction generators (DFIGs) or doubly fed asynchronous generators. A schematic is provided in Figure 1.

The accuracy of system studies depends on the fidelity of the underlying models [6, 7]. Accordingly, the modelling of type-3 WTGs has received considerable attention, see [1, 8, 9, 10, 11, 12] and references therein. Turbine manufacturers routinely develop and maintain accurate models for their products, though disclosure of those models is highly restricted. In some cases they have released models that describe functionally similar behaviour [13], though such practise is not common. Regional reliability organizations need to exchange models and data that are relevant to their jurisdiction. This has motivated the development of generic models that can be used to capture the functional characteristics of a wide variety of type-3 WTGs [14, 15, 16].

As indicated in Figure 1, the electrical characteristics of type-3 WTGs are governed by interactions between the wound-rotor induction machine and the back-to-back inverter. The inverter excites the rotor of the induction machine with a variable AC source. This provides control of the rotor flux frequency, enabling the rotor shaft frequency to optimally track wind speed [17]. The inverter response time is very fast relative to electromechanical time constants. As a result, the natural dynamics of the induction machine are largely masked from the power system. The dynamic behaviour of a type-3 WTG, as seen from the grid, is therefore dominated by controller response rather than physical characteristics. This is in marked contrast to traditional synchronous generators, where behaviour is governed by device physics.

Controller limits play an integral role in the dynamic performance of type-3 WTGs, with further details provided in Section 2.2. Intrinsic interactions between continuous dynamics and limit-induced discrete events suggest that type-3 WTGs may be classified as hybrid dynamical systems [18, 19, 20]. It will be shown in Section 2.3 that the resulting hybrid dynamics may, in fact, lead to unusual forms of behaviour. The hybrid nature of dynamics also has implications for small disturbance studies.

The studies presented in this chapter focus on the WECC generic type-3 model [15, 16]. This model has been chosen because it is widely used, and is indicative of type-3 models that are generally available. All such generic models are an approximation of the actual dynamics exhibited by a WTG. It is important, though, that this approximation reflects the physical reality of the modelled device.

The chapter is organized as follows. Section 2.2 provides a thorough description of the WECC type-3 WTG model. It is shown in Section 2.3 that non-windup limiter models may cause switching deadlock, preventing trajectory continuation in the usual sense. Alternative

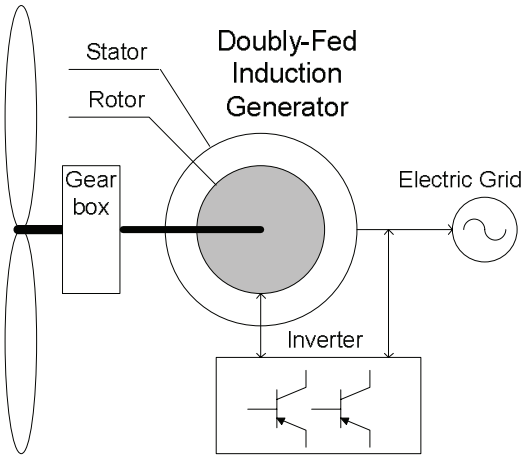

Figure 1: Schematic diagram of a type-3 wind turbine generator.

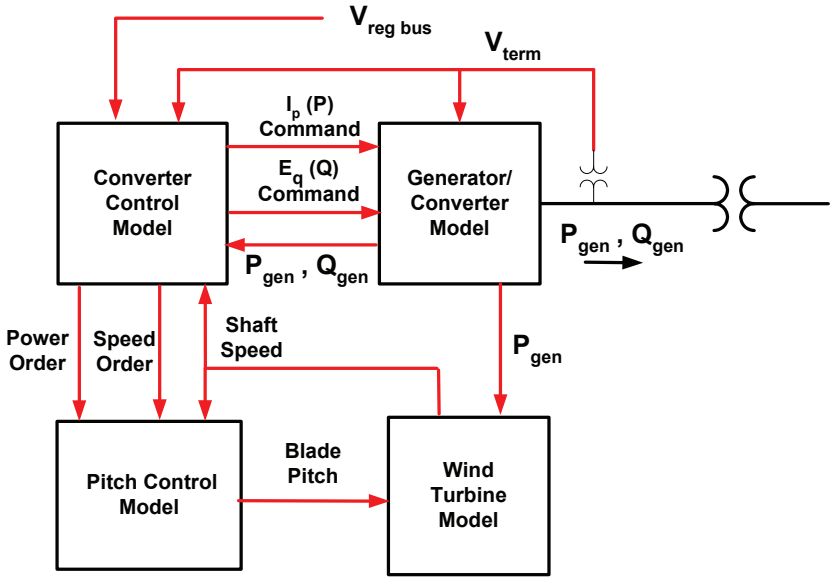

Figure 2: Type-3 WTG dynamic model connectivity, from [15, 16].

model formulations that circumvent such behaviour are discussed. Section 2.4 shows that the model allows multiple equilibria, and discusses the implications. Small disturbance analysis is considered in Section 2.5, and conclusions are presented in Section 2.6.

2.2 Type-3 WTG model

The WECC type-3 wind turbine generator model is defined in [15, 16]. The complete WTG model is divided into four functional blocks, as indicated in Figure 2. This chapter is primarily concerned with the dynamic interactions of the converter control model WT3E, the pitch control model WT3P, and the wind turbine model WT3T. Accordingly, only those models are described in detail in the following analysis.

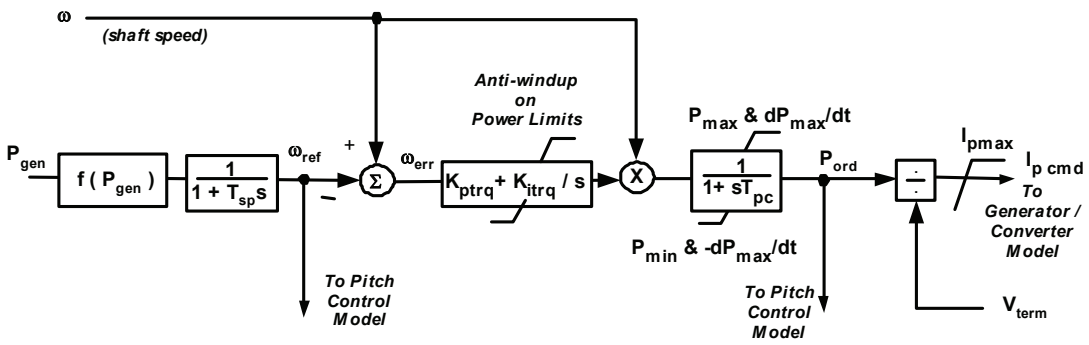

Figure 3: Converter control model WT3E, from [15, 16].

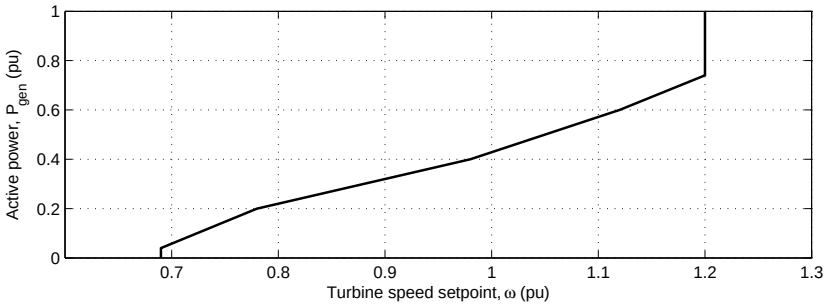

Figure 4: Speed-power relationship, $f(P_{gen})$.

2.2.1 Converter control model WT3E

The converter control model is composed of separate active and reactive power control functions. Reactive power control is very fast, due to the power electronic converter. This chapter focuses on the slower dynamics associated with interactions between active power (torque) control, pitch control, and the coupling through the shaft dynamics. Accordingly, only the active power model, which is shown in Figure 3, will be discussed. Again, full details of the reactive power controller are provided in [15, 16].

The non-windup (anti-windup) limits on the PI block in the centre of Figure 3 are driven by the non-windup P_{max}/P_{min} limits associated with the P_{ord} lag block. The model documentation stipulates that:

(i) If P_{ord} is on its P_{max} limit and ω_{err} (the input to the PI block) is positive, then the K_{itrq}-integrator is blocked, i.e., the state T_ω of that integrator is frozen.

(ii) If P_{ord} is on the P_{min} limit and ω_{err} is negative, then the K_{itrq}-integrator state is frozen.

This form of non-windup limit is unusual, though a precedence can be found in Annex E.5 of IEEE Standard 421.5-2005 [21]. It will be shown in Section 2.3 that such non-windup logic can result in switching deadlock [22].

The function $f(P_{gen})$ is typically modelled as a piece-wise affine function. WECC default parameters, which are provided in Appendix C, produce the curve shown in Figure 4.

Assembling all the equations for the model gives,

$$\frac{d\omega_{ref}}{dt} = \frac{1}{T_{sp}}\Big(f(P_{gen}) - \omega_{ref}\Big) \tag{1}$$

$$\frac{dT_{\omega}}{dt} = K_{itrq}(\omega - \omega_{ref}) \times y_{freeze} \tag{2}$$

$$\frac{dP_{ord}}{dt} = P_{ord,rtlm} \times y_{mx,sw} \times y_{mn,sw} \tag{3}$$

$$P_{ord,rate} = \frac{1}{T_{pc}}\Big(\omega\big(T_{\omega} + K_{ptrq}(\omega - \omega_{ref})\big) - P_{ord}\Big) \tag{4}$$

together with the switched equations (97)-(100) that are given in Appendix A.

The value of the model (1)-(4) and (97)-(100) is that it provides a precise, unambiguous description of dynamic behaviour. This level of detail is vitally important for analyzing the model idiosyncracies that are discussed in later sections.

2.2.2 Pitch control model WT3P

The pitch control model WT3P is shown in Figure 5. Of particular interest is the implementation of the non-windup limiter on the pitch angle θ. As stated in the model documentation,

> "The Pitch Control and Pitch Compensation integrators are non-windup integrators as a function of the pitch, i.e., the inputs of these integrators are set to zero when the pitch is in limits (PI_{max} or PI_{min}) and the integrator input tends to force the pitch command further against its limit."

To illustrate, consider the case where θ is on its lower limit PI_{min}. A negative input to the pitch-control integrator would cause the corresponding state x_p to reduce, which in turn would force θ further against its PI_{min} limit. To prevent that wind-up effect, the integrator is blocked under such conditions. Similarly, the pitch-compensation integrator is blocked when its input is negative. When θ is on its upper limit PI_{max}, blocking of the up-stream integrators occurs when their respective inputs are positive.

This blocking philosophy is the same as that employed in the converter control model WT3E, as discussed in Section 2.2.1. It should again be mentioned that such blocking can result in switching deadlock. This will be explored in Section 2.3.

The equations describing the WT3P model can be written,

$$\frac{dx_p}{dt} = K_{ip}\big(\omega - \omega_{ref}\big) \times y_{fr,1} \tag{5}$$

$$\frac{dx_c}{dt} = K_{ic}\big(P_{ord} - P_{set}\big) \times y_{fr,2} \times y_{sw} \tag{6}$$

$$\frac{d\theta}{dt} = \theta_{rtlm} \times y_{mx,sw} \times y_{mn,sw} \tag{7}$$

$$\theta_{rate} = \frac{1}{T_{PI}}\big(\theta_{cmd} - \theta\big) \tag{8}$$

$$\theta_{cmd} = x_p + x_c + K_{pp}\big(\omega - \omega_{ref}\big) + K_{pc}\big(P_{ord} - P_{set}\big) \tag{9}$$

along with the switched equations (101)-(106) that are provided in Appendix B.

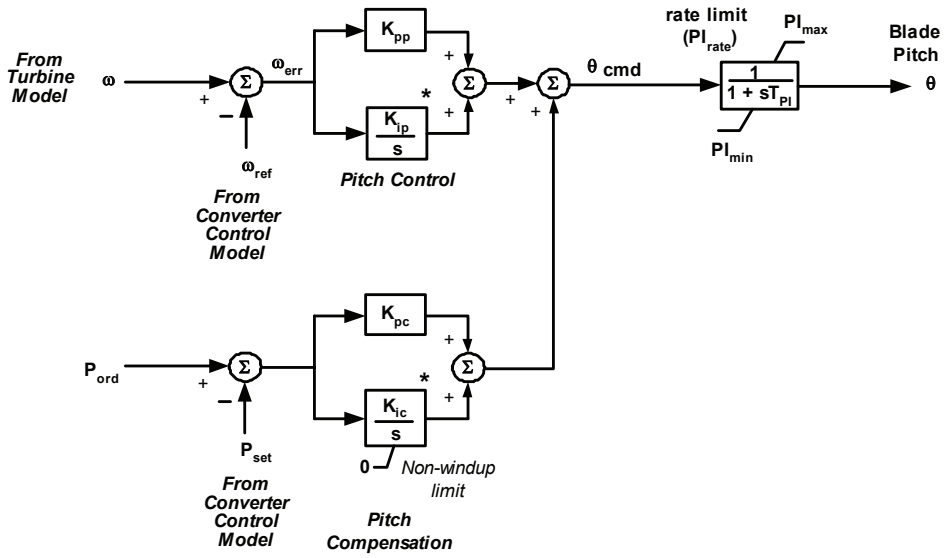

Figure 5: Pitch control model WT3P, from [15, 16].

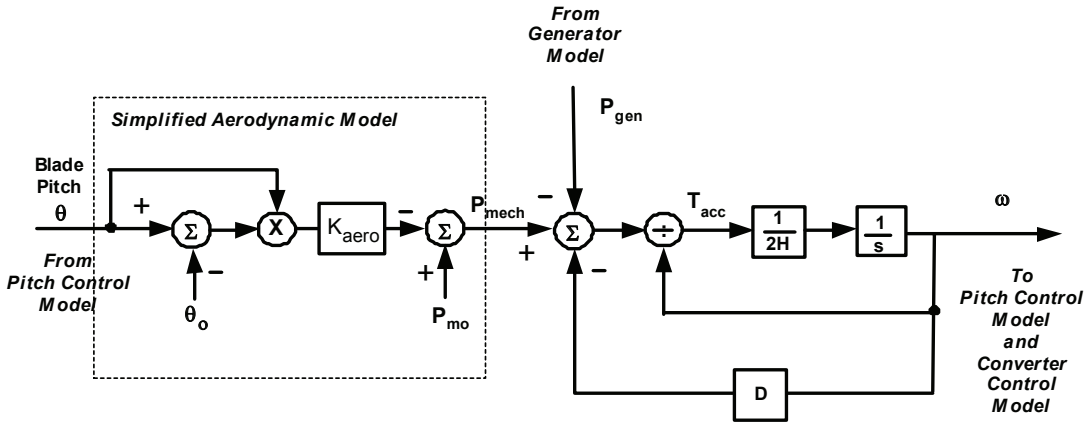

Figure 6: Single-mass turbine model WT3T, from [15, 16].

2.2.3 Wind turbine model WT3T

The single-mass wind turbine model WT3T from [15, 16] is shown in Figure 6. A two-mass model is also provided in [15, 16], but the single-mass model suffices for the discussions in this chapter. The model consists of two parts, 1) a simplified model of the aerodynamic relationship between blade pitch θ and mechanical power P_{mech}, and 2) a model of the shaft dynamics. The damping constant D is always zero, so the single-mass WT3T model can be described by,

$$\frac{d\omega}{dt} = \frac{1}{2H\omega}\big(P_{mech} - P_{gen}\big) \tag{10}$$

$$P_{mech} = P_{mo} - K_{aero}\theta\big(\theta - \theta_o\big). \tag{11}$$

2.2.4 Hybrid system model

It is clear from (1)-(11) and (97)-(106) that the WTG model is composed of:

i) Differential and algebraic equations that describe continuous behaviour of the associated states, and

ii) Discrete events that introduce nonsmooth behaviour through switching actions.

Models that involve such interactions between continuous dynamics and discrete events have become known as hybrid dynamical systems [18, 19, 20]. The discrete events introduce rich forms of behaviour that are not exhibited by smooth systems described by differential (and possibly coupled algebraic) equations. In fact, it will be shown in Section 2.3 that both the WT3E and WT3P models are susceptible to switching deadlock, where a discrete state should simultaneously take two different values. This situation is impossible, of course; the trajectory is not defined (in the usual sense) beyond such an impasse.

The WTG model (1)-(11), (97)-(106) has been formulated according to the differential-algebraic impulsive switched (DAIS) structure described in [20, 23]. A subtle (but technically important) modification was required however. In the original DAIS definition, switched algebraic equations had the form

$$0 = \begin{cases} g^+(x,y), & y_s > 0 \\ g^-(x,y), & y_s < 0 \end{cases}$$

where behaviour is undefined if the trigger variable y_s remains at zero. In the case of a WTG though, it is quite common for the pitch angle θ to be initialized on its lower limit PI_{min}. To cater for that (and similar) situations, the DAIS definition has been altered to allow the trigger variable y_s to remain at zero, giving the slightly modified switching description,

$$0 = \begin{cases} g^+(x,y), & y_s \geq 0 \\ g^-(x,y), & y_s < 0. \end{cases}$$

In the case of the non-windup limits within the WTG model, (98)-(99) and (102)-(104), it has been arbitrarily decided that the integrator should remain active when its state lies on the limit, i.e., when the trigger variable $y_s = 0$. The integrator only becomes blocked when the input seeks to force the state across the limit, resulting in $y_s < 0$.

Technical issues arise when an equilibrium point coincides with a switching condition $y_s = 0$. If the equilibrium is asymptotically stable, then generically, as the trajectory approaches the equilibrium point, the time between subsequent switching events will progressively diminish. In the limit, switching will (theoretically) become infinitely fast. Also, linearization about the equilibrium point is not defined, as the vector field is not smooth. Consequently, small disturbance analysis is not possible. This latter point is explored further in Section 2.5.

2.3 Trajectory deadlock

2.3.1 Background

Conceptually, deadlock refers to the situation where a trajectory encounters a condition that precludes further progress. Such behaviour is unusual for systems described by continuous

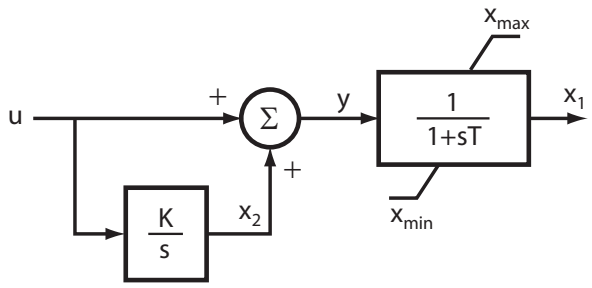

Figure 7: Simplified representation of non-windup limited block and upstream PI controller.

dynamics[1], though differential-algebraic systems can experience deadlock in the form of algebraic singularity[2] [25, 26].

Hybrid dynamical systems, on the other hand, are more prone to deadlock, due to their inherent interactions between continuous dynamics and discrete events. In this context, deadlock has been formally defined in [22]. The form of deadlock of particular relevance to WTG modelling is known as *chattering Zeno*, which refers to situations where "the discrete component infinitely jumps instantaneously between different domains, while the continuous component remains unchanged" [22]. Subsequent sections describe this behaviour in the context of the type-3 WTG model, and provide an alternative model formulation that alleviates the deadlock phenomenon.

It should be noted that because deadlock precludes continuation of a trajectory, numerical simulation techniques that accurately capture hybrid system dynamics cannot proceed beyond the deadlock point. Conversely, simulators that continue through deadlock cannot be truly implementing the hybrid system model. Special techniques have been developed for continuing approximate solutions beyond deadlock, with Filippov solution concepts forming the basis for those methods [27]. Such concepts are required, for example, in analyzing sliding mode behaviour [28]. They are not pursued in this chapter.

2.3.2 Deadlock in WTG models

The switching logic that gives rise to trajectory deadlock in the type-3 WTG model can be explained with the aid of the simplified model of Figure 7. Referring to Figure 5, it can be seen that this reduced model is equivalent to the output lag block and one of the upstream PI regulators of the WT3P model.

Consider the case where x_1 is on its lower limit x_{min}, and the input u is negative. According to the non-windup logic of WT3P, the x_2-integrator would be blocked. Assume that u is increasing, though remains negative. This increase in u will translate directly into an increase in y, as x_2 is constant. With increasing y, conditions conducive to deadlock occur when y reaches $x_1 = x_{min}$. This may be explained by noting that $\dot{x}_1 = (y - x_1)/T$, and hence $\dot{x}_1 = 0$ at the point where y encounters $x_1 = x_{min}$. The evolution of x_1 from that point is therefore governed by $\ddot{x}_1$, which can be written

$$\ddot{x}_1 = \frac{1}{T}(\dot{y} - \dot{x}_1) = \frac{1}{T}\dot{y} = \frac{1}{T}(\dot{u} + \dot{x}_2).$$

[1]Technically, deadlock cannot occur if the vector field is Lipschitz [24].

[2]In this case, the term *impasse* is often used rather than deadlock.

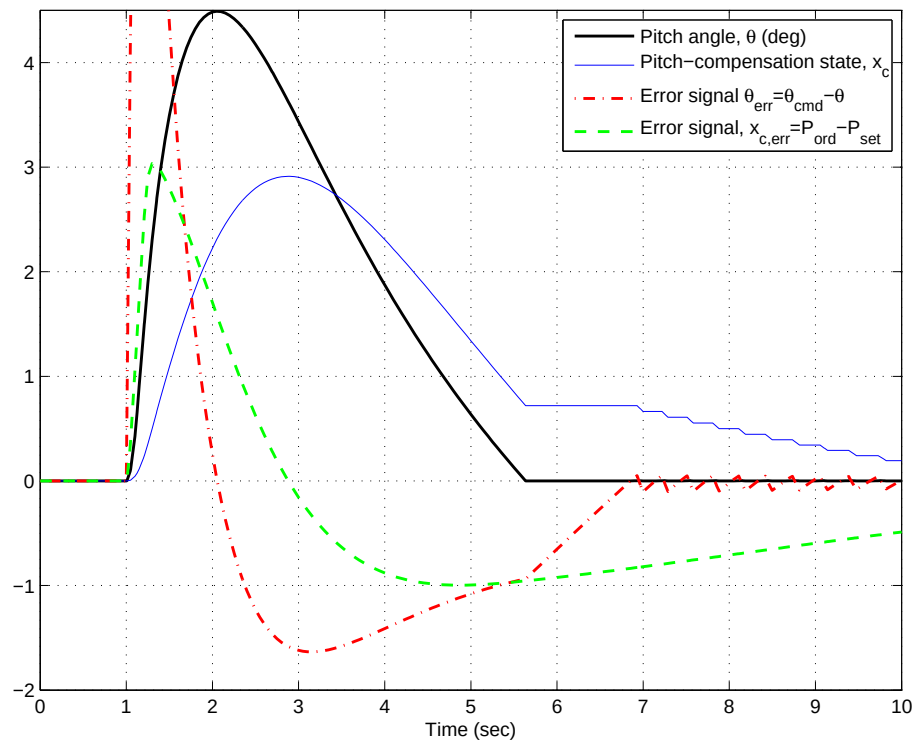

Figure 8: Large-disturbance response of pitch states.

If the x_2-integrator is blocked, $\dot{x}_2 = 0$, giving $\ddot{x}_1 = \frac{1}{T}\dot{u} > 0$ because u is increasing. In this case, x_1 will tend to increase away from the x_{min} limit, and the x_2-integrator will become unblocked. On the other hand, if the x_2-integrator is unblocked, the sign of $\ddot{x}_1$ is given by $\dot{u} + \dot{x}_2 = \dot{u} + Ku$, which may be negative. If so, x_1 will tend to decrease onto the x_{min} limit, blocking the x_2-integrator. A contradiction arises: if the x_2-integrator is blocked it should unblock, but if it's unblocked it should block.

Returning to the type-3 WTG model, this deadlock phenomenon can be illustrated using the WECC test system and default parameters that are provided in Appendix C. Resulting trajectories are shown in Figure 8. For the sake of clarity, only the pitch-compensation integrator will be discussed, though the pitch-control integrator exhibits similar behaviour. It should be noted that in order to generate the trajectories shown in Figure 8, it was necessary to introduce hysteresis into the switching process associated with the pitch angle non-windup limit. The implementation of hysteresis is discussed in Section 2.3.3.

The pitch angle θ is initially in steady-state on the lower non-windup limit, where $\theta_0 = PI_{min} = 0$ deg. In response to the disturbance, θ undergoes a transient increase, before returning to PI_{min} at 5.6 sec. The error signal $x_{c,err} = P_{ord} - P_{set}$ driving the pitch-compensation integrator is negative at that time, so the corresponding state x_c is frozen. Over the subsequent period, θ and x_c remain frozen, but the signal $\theta_{err} = \theta_{cmd} - \theta$, which drives variations in θ, steadily increases until reaching zero[3] at around 7 sec. At that point, θ should transition from blocked to unblocked, so the pitch-compensation integrator driving x_c should also

[3]The hysteresis implementation actually allows θ_{err} to rise a little beyond zero before the x_c-integrator is unblocked. Further details are provided in Section 2.3.3.

unblock. But notice that $x_{c,err}$ is negative, so as soon as the integrator unblocks, x_c will decrease, driving θ_{err} negative. This forces θ back onto its PI_{min} limit, blocking x_c again. But with x_c blocked, θ_{err} increases above zero, and x_c is unblocked. Without hysteresis, this process would repeat *ad infinitum*.

In summary, at the point where θ_{err} encounters zero,

- If θ is blocked, then θ and x_c should unblock.
- If θ is unblocked, then θ and x_c should block.

In other words, at the instant when $\theta_{err} = 0$, the discrete state describing integrator blocking undergoes infinitely many switches, preventing the continuation of the trajectory. This impasse can be circumvented by implementing hysteresis in the blocking/unblocking process, as described in the following section.

It should be mentioned that this example was not concocted to highlight deadlock, but is just the WECC test system with default parameters [15, 16]. Similar behaviour has been observed in studies of numerous other systems, suggesting deadlock situations are not uncommon. It should be kept in mind, though, that this is an artifact of the simplified modelling, and is not observed in real WTGs.

2.3.3 Implementation of hysteresis

The explanation of hysteresis will refer to Figure 9. This is an expanded view of the relevant time interval of Figure 8. In order to provide a clearer view of behaviour, however, the hysteresis band has been widened from 0.002 in Figure 8 to 0.05 in Figure 9.

At 6.85 sec, the error signal θ_{err} crosses through zero. Upon doing so, the integrator driving the pitch angle θ is unblocked, so θ begins to increase. At 7.3 sec, θ encounters the hysteresis threshold, whereupon the pitch-compensation integrator is unblocked. The error signal $x_{c,err}$ driving that integrator is negative, as shown in Figure 8, so x_c immediately begins to reduce. This causes θ_{err} to reduce. Eventually θ_{err} goes negative, and θ begins to fall, encountering the non-windup limit $PI_{min} = 0$ at 7.6 sec. When that limit is encountered, θ and x_c are immediately blocked, so θ_{err} again begins to increase. The process then repeats. The actual implementation of the hysteresis logic is presented in [29].

The width of the hysteresis band ϵ influences behaviour during the deadlock period, but has little effect on the subsequent trajectory. This influence was explored using trajectory sensitivities [30]. Figure 10 shows the sensitivity of the θ and x_c trajectories to a one percent change in the nominal width $\epsilon = 0.002$ of the hysteresis band. It can be seen that the effect of the perturbation in ϵ accumulates over the deadlock period, but subsequently decays very quickly. Choosing a suitable value for ϵ results in a tradeoff between the magnitude of the chatter during the deadlock period versus the number of switching operations.

2.4 Equilibrium conditions

2.4.1 Initialization

For the initial point to be in equilibrium, the derivatives in (1)-(3), (5)-(7) and (10) must be set to zero. Notice though that because (2) and (5) are effectively duplicate integrators, they both contribute exactly the same equilibrium equation, $\omega - \omega_{ref} = 0$. The redundant equation will be ignored when assembling the complete set of initialization equations.

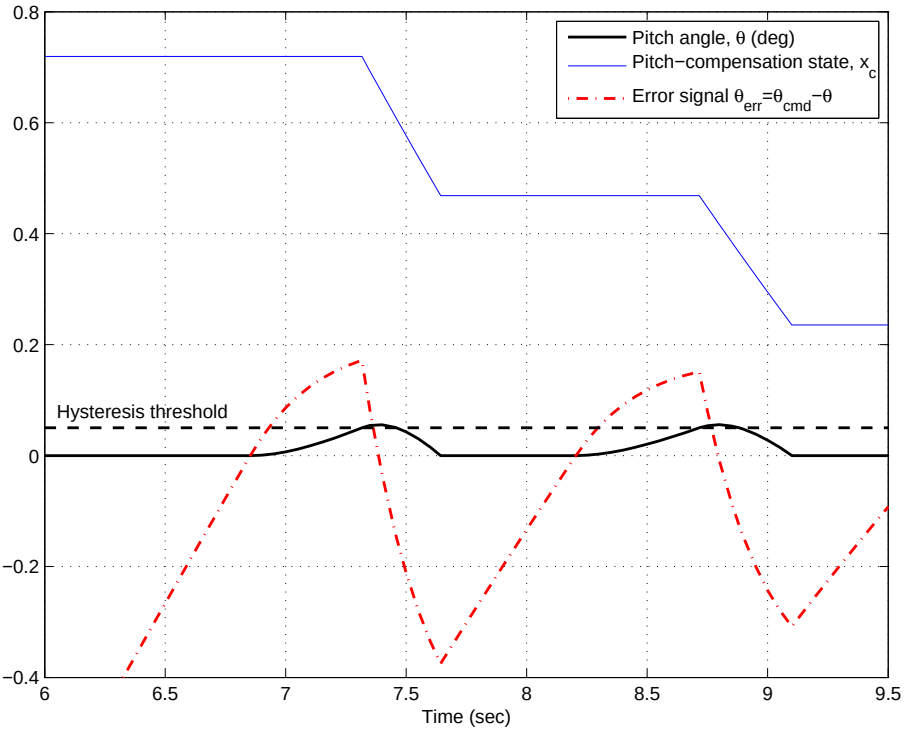

Figure 9: Expanded view of hysteresis behaviour.

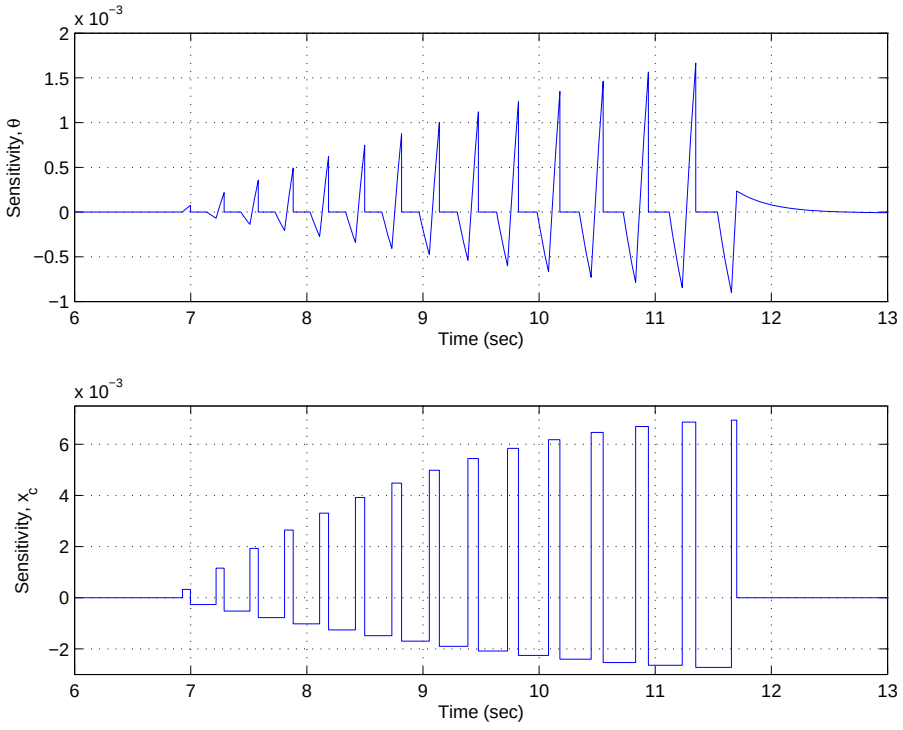

Figure 10: Sensitivity of θ and x_c trajectories to a one percent change in the width ϵ of the hysteresis band.

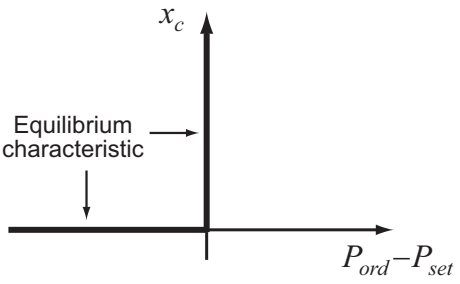

Figure 11: Equilibrium characteristic for the pitch compensation integrator.

The status of the switched equations must also be consistent with equilibrium conditions. It is safe to assume that none of the limits in the converter control model WT3E would be active during normal steady-state operation. Under that assumption, P_{ord} will equal the electrical power P_{gen} delivered to the WTG terminal bus. This relationship will be used to eliminate P_{gen} from the equilibrium equations.

In the case of the pitch control model WT3P, limits may be active at steady-state. For wind conditions up to rated wind-speed, the pitch angle θ would normally sit at its minimum limit PI_{min}. Blocking the associated integrator would, however, leave the initial value of θ_{cmd} undefined. The initialization process must therefore override integrator blocking, or equivalently, assume θ lies infinitesimally above the PI_{min} limit.

The pitch compensation non-windup limiter of WT3P has the equilibrium characteristic shown in Figure 11. If the input $P_{ord} - P_{set} < 0$ at steady-state, then x_c will be forced to its lower limit of zero. On the other hand, if $P_{ord} - P_{set} = 0$ at steady-state, then x_c may take any non-negative value. Summarizing this relationship gives,

$$x_c \geq 0, \quad P_{set} - P_{ord} \geq 0, \quad x_c(P_{set} - P_{ord}) = 0,$$

which is a complementarity condition [31, 32] that can be expressed compactly using standard notation,

$$0 \leq x_c \perp (P_{set} - P_{ord}) \geq 0. \tag{12}$$

The resulting initialization equations can be written,

$$0 = f(P_{ord}) - \omega_{ref} \tag{13}$$
$$0 = \omega - \omega_{ref} \tag{14}$$
$$0 = \omega T_\omega - P_{ord} \tag{15}$$
$$0 = P_{mo} - K_{aero}\theta\big(\theta - \theta_o\big) - P_{mech} \tag{16}$$
$$0 = P_{mech} - P_{ord} \tag{17}$$
$$0 = x_p + x_c + K_{pc}\big(P_{ord} - P_{set}\big) - \theta_{cmd} \tag{18}$$
$$0 = \theta_{cmd} - \theta \tag{19}$$

together with (12). The dependent state variables are ω_{ref}, T_ω, P_{ord}, x_p, x_c, θ, ω, θ_{cmd} and P_{mech}, while K_{aero}, K_{pc}, P_{mo} and P_{set} are parameters. By definition, θ_o is the specified initial value for the pitch angle θ, thereby providing a further initialization equation,

$$\theta - \theta_o = 0. \tag{20}$$

Because P_{mo} and P_{set} are independent parameters, it is important to consider initialization for the three cases, $P_{mo} < P_{set}$, $P_{mo} = P_{set}$ and $P_{mo} > P_{set}$. To do so, first notice that (16)-(17) and (20) together infer $P_{mo} = P_{ord}$ at initialization. Therefore, for the case $P_{mo} = P_{ord} < P_{set}$, the complementarity condition (12), expressed visually in Figure 11, ensures that $x_c = 0$. In the second case, when $P_{mo} = P_{ord} = P_{set}$, (12) only specifies that $x_c \geq 0$. It follows that the initialization description consists of only eight independent equations describing nine variables. The set of equations is under-determined. This can be confirmed by noting that x_c and x_p appear only in (18), and therefore cannot be uniquely determined. To resolve this situation, (12) should be replaced at initialization by an equation that assigns a specific initial value to x_c or x_p. For consistency with the $P_{mo} < P_{set}$ case, it is convenient to replace (12) by

$$x_c = 0. \tag{21}$$

The third case $P_{mo} = P_{ord} > P_{set}$ implies the integrator would be driven by a sustained positive input. The WT3P model does not define an upper limit though, so equilibrium could not be achieved.

2.4.2 Post-disturbance steady-state

For well-posed dynamical models, the post-disturbance steady-state should match the pre-disturbance (initial) equilibrium when pre- and post-disturbance parameter sets are identical. This is generically not the case for the WECC type-3 WTG model. The following analysis shows that this unusual behaviour is due to switching associated with the duplicate integrators (2) and (5).

The initialization equations (12)-(19) govern post-disturbance steady-state conditions, as they were obtained by setting derivatives to zero. Initialization also made use of the auxiliary equation (20), but that equation plays no role as the system evolves towards steady-state. As a consequence of discarding (20), the description of steady-state conditions is under-determined.

This indeterminacy is resolved when the duplicate integrators (2) and (5) remain unblocked for the entire time horizon. In that case, the integrator states can be written in integral form,

$$T_\omega(t) = T_\omega^o + K_{itrq} \int_0^t \big(\omega(\tau) - \omega_{ref}(\tau)\big) d\tau \tag{22}$$

$$x_p(t) = x_p^o + K_{ip} \int_0^t \big(\omega(\tau) - \omega_{ref}(\tau)\big) d\tau \tag{23}$$

where T_ω^o and x_p^o are the initial values for the respective states. Equating the integrals in (22) and (23) gives the affine relationship,

$$x_p(t) = \frac{K_{ip}}{K_{itrq}} T_w(t) + \left(x_p^0 - \frac{K_{ip} T_w^0}{K_{itrq}} \right) \tag{24}$$

which implies that any variation in $T_\omega(t)$ will be matched by a corresponding variation in $x_p(t)$. This relationship provides the extra equation required to uniquely determine the post-disturbance steady-state, and in fact implies that if all parameters remain unchanged, the system will evolve to a steady-state that exactly matches the initialization point.

The assumption that the duplicate integrators remain unblocked for all time is seldom true, however. Blocking of one or other of the integrators will alter the corresponding integral

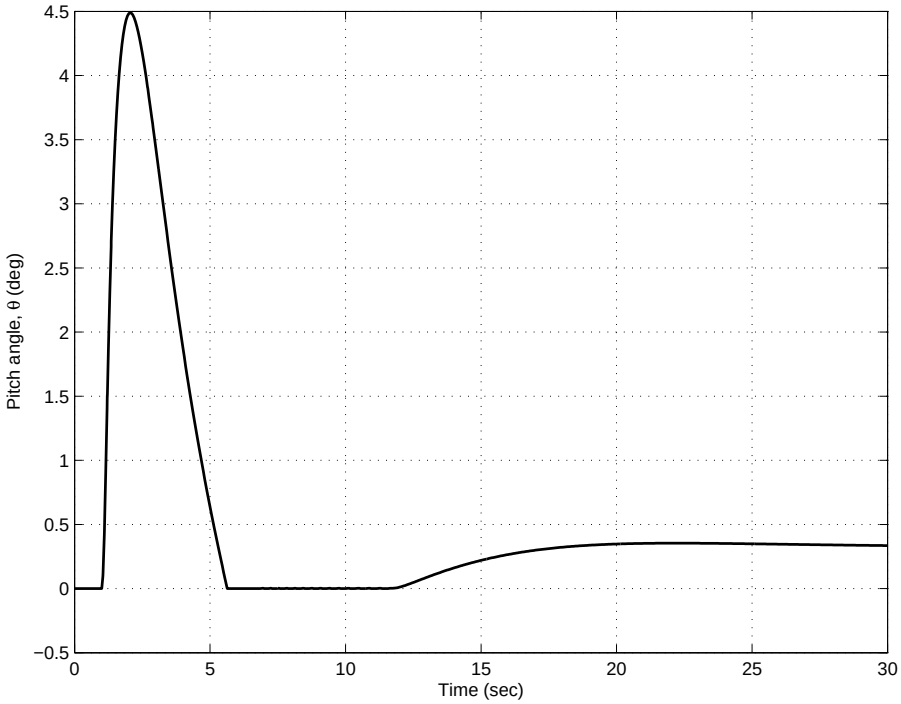

Figure 12: Large-disturbance response of pitch angle θ.

term in (22) or (23), invalidating the relationship (24). Under such conditions, it becomes impossible for both T_ω and x_p to evolve back to their initial values. Consequently, the system will settle to a post-disturbance steady-state that cannot equal the initial point, even though the parameters of the system are unchanged.

The WECC test system and default parameters of Appendix C illustrate this phenomenon. The pitch angle response of Figure 8 is repeated in Figure 12, where the time horizon has been extended to 30 seconds. Notice that the pitch angle evolves to a steady-state value of 0.33 deg, even though it was initialized at 0 deg.

Figure 13 shows the relationship between T_ω and x_p. These two states initially follow a straight line given by (24), with the states reaching the extreme point $(T_\omega, x_p) = (0.847, 0.56)$, before returning along the line to $(0.835, 0.08)$. At that instant, the pitch angle θ encounters its limit, causing the integrator driving x_p to block. The integrator remains blocked until θ enters a period where hysteresis is active. During that period, the x_p-integrator successively blocks and unblocks, giving rise to the staircase phenomenon apparent in the figure. At the end of that period, θ finally comes off its limit, the x_p-integrator is restored to normal operation, and the behaviour of T_ω and x_p reverts to a straight-line locus given by an affine relationship like (24). The slope over that final section is the same as earlier, but the offset has changed. Hence the system converges to a steady-state that differs from the starting equilibrium point.

As was the case with deadlock, this situation is a consequence of simplified modelling, and does not occur in actual WTGs.

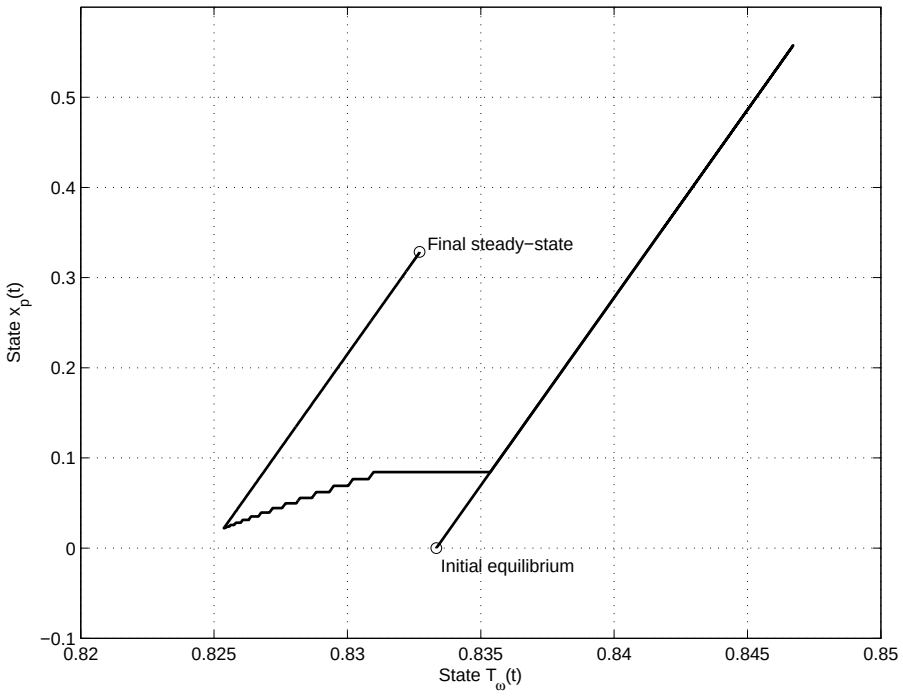

Figure 13: Relationship between $T_\omega(t)$ and $x_p(t)$.

2.5 Small disturbance analysis

2.5.1 Singularity

Linearizing the WTG equations (1)-(11) about an equilibrium point, and eliminating the algebraic equations, yields the seventh-order linear model,

$$\frac{d}{dt}\begin{bmatrix}\Delta\omega_{ref}\\ \Delta T_\omega\\ \Delta P_{ord}\\ \Delta x_p\\ \Delta x_c\\ \Delta\theta\\ \Delta\omega\end{bmatrix} = \begin{bmatrix} a_{11} & . & a_{13} & . & . & . & . \\ a_{21} & . & . & . & . & . & a_{27} \\ a_{31} & a_{32} & a_{33} & . & . & . & a_{37} \\ a_{41} & . & . & . & . & . & a_{47} \\ . & . & a_{53} & . & . & . & . \\ a_{61} & . & a_{63} & a_{64} & a_{65} & a_{66} & a_{67} \\ . & . & a_{73} & . & . & a_{76} & . \end{bmatrix}\begin{bmatrix}\Delta\omega_{ref}\\ \Delta T_\omega\\ \Delta P_{ord}\\ \Delta x_p\\ \Delta x_c\\ \Delta\theta\\ \Delta\omega\end{bmatrix} \tag{25}$$

where the a_{ij} refer to elements of the system A-matrix that are potentially non-zero, while all other elements are identically zero. The exact arrangement of the non-zero a_{ij} is dependent upon the status of limits.

As in Section 2.4, it is assumed that none of the limits in the converter control model WT3E are enforced at steady-state, and that pitch angle θ dynamics are active. In the case of the pitch compensation x_c-integrator, its dynamics may be active at steady-state or the limiter may be enforced, as indicated in Figure 11. Both situations must be considered.

The initial value θ_o for the pitch angle also has an important influence on the linear model. When (11) is linearized with $\theta_o = 0$, the term associated with the simplified aerodynamic model becomes zero. In that case, perturbations in the pitch angle θ have no influence on P_{mech}, and as a consequence $a_{76} = 0$ in (25). On the other hand, when $\theta_o \neq 0$, the aerodynamic model contributes a non-zero term to (11), resulting in $a_{76} \neq 0$.

In considering the various cases identified above, it should be kept in mind that (2) and (5) are duplicate integrators. Because these integrators differ only by a scaling factor, the corresponding rows of the A-matrix, 2 and 4 respectively, are linearly dependent. Therefore A must have at least one eigenvalue whose value is zero.

The two conditions for the x_c-integrator, together with the two possibilities for θ_o, give four separate cases:

Case 1: x_c-integrator active, $\theta_o \neq 0$. The condition $\theta_o \neq 0$ implies $a_{76} \neq 0$, so all the a_{ij} shown in (25) are non-zero. The A-matrix has a single zero eigenvalue due to the linear dependence of rows 2 and 4, which correspond to the duplicate integrators. By inspection, columns 4 and 5 are linearly dependent, implying that the right eigenvector associated with the zero eigenvalue involves only Δx_p and Δx_c. Substituting that zero-eigenvector[4] into (25) gives a matrix-vector product that is zero. Hence, the linear system will be in steady-state at any point along the zero-eigenvector.

Case 2: x_c-integrator active, $\theta_o = 0$. In this case $\theta_o = 0$ so $a_{76} = 0$. By inspection, rows 5 and 7 are linearly dependent, as well as rows 2 and 4, implying the system now has two eigenvalues that are zero. This second zero-eigenvalue is a consequence of pitch angle $\Delta\theta$ being decoupled from mechanical power ΔP_{mech} when $\theta_o = 0$ in the simplified aerodynamic model. With $a_{76} = 0$, columns 4, 5 and 6 are clearly linearly dependent. The two zero-eigenvectors in this case involve Δx_p, Δx_c and $\Delta\theta$. The linear system will be in steady-state at any point on the plane spanned by the two zero-eigenvectors.

Case3: x_c-integrator blocked, $\theta_o \neq 0$. Blocking the x_c-integrator implies $\Delta x_c \equiv 0$. Accordingly, the fifth row and column of the A-matrix should be removed, reducing the linearized system to six dynamic states. The linear dependence of rows 2 and 4 is unaffected by this reduction, so one of the eigenvalues remains zero. Because $a_{76} \neq 0$, no simple pairing of columns produces linear dependence. In fact, linear dependence involves all the columns of the reduced A-matrix. Accordingly, the zero-eigenvector includes a contribution from all six states of the reduced model.

Case 4: x_c-integrator blocked, $\theta_o = 0$. This case also has $\Delta x_c \equiv 0$, so the A-matrix is again reduced. Because $\theta_o = 0$, the element $a_{76} = 0$, and by inspection the columns corresponding to Δx_p and $\Delta\theta$ are linearly dependent. The zero-eigenvector therefore involves only Δx_p and $\Delta\theta$.

2.5.2 Eliminating the zero eigenvalue

It is possible to eliminate the zero eigenvalue caused by integrator duplication by exploiting the explicit coupling between integrator states T_ω and x_p given by (24). Linearizing that affine relationship gives

$$\Delta x_p(t) = \frac{K_{ip}}{K_{itrq}} \Delta T_w(t). \tag{26}$$

In the linearized model (25), removing the row corresponding to Δx_p, and replacing all occurrences of Δx_p by (26), reduces the system dimension by one. It can be shown that the remaining eigenvalues are exactly the same as the original non-zero eigenvalues. If those

[4]For convenience, the right eigenvector associated with the zero eigenvalue will be referred to as the zero-eigenvector.

original non-zero eigenvalues all have negative real parts, as is generically the case, the system will be exponentially stable.

Even though the linear model has a continuum of equilibria defined by the zero-eigenvector, perturbations that satisfy (26) will induce behaviour that returns to the original equilibrium point. On the other hand, perturbations that do not satisfy (26) will result in convergence to points on the zero-eigenvector that generically differ from the original point.

2.5.3 Linearizing at limits

Linearization about an equilibrium point requires the dynamical system to be smooth in a neighbourhood of that point. With hybrid dynamical systems, such as the WTG model, equilibria may coincide with conditions that induce switching. In such cases, it is impossible to find a neighbourhood of the equilibrium point where the dynamical system is smooth. Linearization is therefore not well defined.

Consider the pitch compensation x_c-integrator, whose equilibrium characteristic is provided in Figure 11. Linearizing about an equilibrium point anywhere on the vertical or horizontal sections of the characteristic, away from the transition point at the origin, is well defined and discussed in Section 2.5.1. At the origin, however, switching will occur as perturbations in x_c transition from positive to zero. To establish a linear model at this point, switching must be disabled. The x_c-limit may be ignored, so the origin behaves like a point on the vertical characteristic, or it may be enforced, in which case the origin will act like a point on the horizontal characteristic. It is important to note that the two cases will result in different linear models, and hence eigen-structures that differ. Neither is strictly correct, and results must be interpreted with great care.

A similar discussion applies for the pitch angle θ dynamics. As mentioned in Section 2.4.1, it is common for θ to be initialized on its lower limit PI_{min}. A choice must be made whether to treat the integrator as active or blocked. The analysis of Section 2.5.1 was based on the assumption that the integrator was active.

The ill-defined nature of linearization at a switching point is particularly important for analysis packages that use finite differences to generate approximate derivatives. Care must be taken to ensure that differences are calculated using perturbations that are physically meaningful. Otherwise the linear model may be quite inaccurate.

2.6 Conclusions

The dynamic behaviour of type-3 WTGs is governed by interactions between a wound-rotor induction machine and a back-to-back inverter. The inverter response time is much faster than the time constants of the induction machine, allowing the inverter to respond rapidly to the electromechanical dynamics of the WTG. Consequently, the dynamic characteristics of a type-3 WTG that are important from the grid perspective are dominated by the response of controllers that regulate active power, pitch angle and terminal voltage. These controllers involve interactions between continuous dynamics of state variables and discrete events that occur when limits are encountered. WTGs may therefore be classed as hybrid dynamical systems.

Non-windup limits within the WECC type-3 WTG model have been structured so that various integrators are blocked when a limit is encountered. The interactions inherent in this model structure can be quite complex, and may lead to a form of trajectory deadlock

known as chattering Zeno. Deadlock precludes continuation of the trajectory in the normal sense, so numerical simulation techniques that accurately capture hybrid system dynamics cannot proceed beyond such a point. Filippov solution concepts are required for continuing the trajectory. It has been shown that deadlock can be eliminated by incorporating hysteresis into the switching of non-windup limits.

The converter controller and the pitch controller of the WECC type-3 WTG model both include an integrator that is driven by the same frequency error signal. This integrator duplication results in an under-determined description of steady-state conditions, allowing the existence of a continuum of equilibria. As a consequence, power systems that incorporate WTGs may converge to a post-disturbance steady-state that does not match initial conditions, even though the parameter set has not changed. Furthermore, the duplicate integrators result in linearly dependent rows in the linearized WTG model, so the system is singular. Small disturbance analysis of power systems with WTGs will yield at least one zero-eigenvalue for every WTG.

3 Wind-Farm Reactive Support and Voltage Control

3.1 Introduction

Utility-scale wind generation facilities should be capable of regulating voltage through the provision of dynamic reactive support [33]. Wind-farms, however, are comprised of many distributed [34] wind turbine generators (WTGs) and therefore exhibit behavior that is vastly different to that of traditional large generators. Nevertheless, from a power system operational point-of-view, wind-farms should offer voltage controllability that is consistent with other forms of generation.

The voltage regulating capability of WTGs varies with generator technology and manufacturer [35]. Type 1 and 2 WTGs are based on induction generators, and have no inherent voltage controllability. Type 3 and 4 WTGs involve power electronic converters, which offer the ability to regulate reactive power, and hence achieve voltage control. For various reasons, this capability is often not utilized in type 3 WTGs. Rather, they are often operated at unity power factor. When reactive power regulation is enabled, WTG reactive power set-points are usually coordinated by a central controller that determines a desirable schedule for all WTGs within the wind-farm.

Wind generation installations typically include a substation that establishes the interconnection between the collector network and the grid. These substations incorporate a variety of equipment to regulate voltage, including capacitors, tap-changing transformers, STATCOMs and static VAr compensators (SVCs). This equipment should be used in the most efficient way to meet operational requirements, though there are often multiple conflicting goals. Furthermore, the interactions between devices can be difficult to predict.

This chapter considers three aspects of reactive power control. Of initial interest is the ability of WTGs to provide reactive power support. It is demonstrated that voltage constraints in the collector network limit the total amount of reactive power that can be supplied to the grid. Consequently, the available reactive power at the collector bus is often much less than the specified capability.

Secondly, the stability of the voltage control system is considered. Each device has its own independent controller. These independent control laws can interact to create unexpected or unstable behaviour. Tap-changing transformers are especially vulnerable. This problem is addressed analytically for a simple system to generate threshold criteria for acceptable behaviour.

The third major issue is the high-level, long-term control of the wind-farm reactive support devices. It is desirable to treat all equipment as an integrated system rather than independent devices in order to meet cost, maintenance, fault tolerance, or other requirements. This strategic control updates slowly (minutes) and involves some form of planning for the hours or days ahead. This is a challenging problem because the optimal decisions are time-dependent. Both the current state of the system and the future demands and requirements must be known to arrive at an optimal solution. Controllers are designed with various levels of future information to study the relative importance of forecasting and future estimation. Deterministic and stochastic dynamic programming are used to develop optimal control algorithms.

The chapter is organized as follows: Section 3.2 describes the example wind-farm used in the analysis. Section 3.3 studies the amount of reactive power that can be provided by the WTGs to the collector bus. Section 3.4 undertakes an analytical investigation to determine when the voltage gain of a tap-changing transformer will unexpectedly change sign, that is,

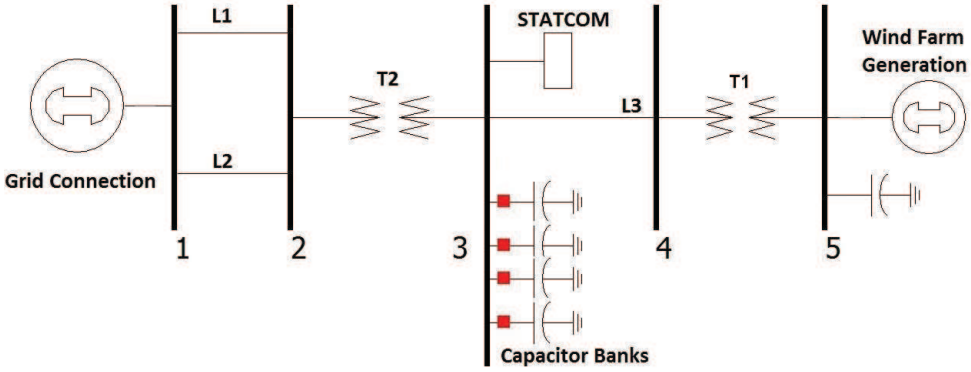

Figure 14: A generic wind-farm layout.

when increasing the tap ratio will decrease the high-side voltage. Section 3.5 analyzes the case where interactions between a tap-changing transformer and a reactive current source can cause instability. Section 3.6 studies the substation-level control problem associated with meeting high-level long-term goals. Finally, conclusions are presented in Section 3.7.

3.2 System Layout and Problem Motivation

A schematic layout of a generic wind-farm is depicted in Figure 14. Turbines may have some form of shunt compensation and a step-up transformer (buses 4 and 5) connecting to a collector system (L3) that transmits power to a substation (buses 2 and 3). Many turbines are connected through a single substation, which typically contains switched capacitors for passive reactive power support, as well as controllable reactive support in the form of SVCs or STATCOMs. A step-up tap-changing transformer T2 connects the substation to the higher-voltage grid, with the strong grid modelled as the infinite bus 1. The various devices associated with buses 2 and 3 are physically located in the same substation, and provide overall reactive power support for the wind-farm.

While the overall layout of the wind-farm is shown in Figure 14, the following sections focus on particular aspects of the reactive power control, and will make simplifying assumptions. Section 3.3 analyzes the collector grid, and Sections 3.4-3.6 focus on the substation. Each section specifies the particular model under consideration.

3.3 Collector system impact on reactive power availability

Type 3 and 4 WTGs employ power electronic converters that allow production or absorption of reactive power. Many WTGs are capable of operating over a power factor range of 0.95 lagging (generating reactive power) to 0.95 leading (absorbing reacting power) at full active power output, for example. Manufacturers specify active/reactive capability curves for their WTGs to describe their exact operational characteristics. Often wind-farm developers use those capability curves directly to determine the total reactive power available at the point of interconnection. Whilst such calculations take into account losses on the collector system, they tend not to consider voltage rises/falls across the collector feeders and WTG step-up

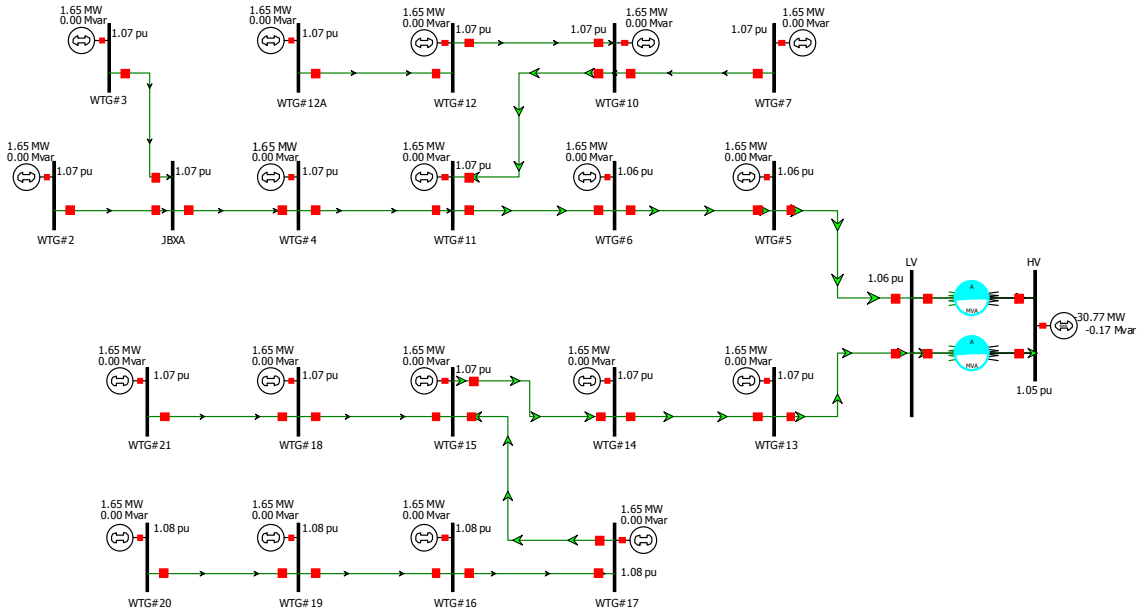

Figure 15: Example wind-farm topology.

transformers. The following discussion shows that as a result, the total reactive power (both lagging and leading) that's available at the collector bus tends to be overstated.

In discussing the restrictions on reactive power that arise due to collector bus voltages, it is convenient to refer to the example system shown in Figure 15. For clarity, the figure does not show the step-up transformers associated with each WTG, though those transformers have been included in the analysis. Also, the discussion focuses on reactive power production (WTGs operating in lagging power factor), though a similar argument holds for reactive power absorption (leading power factor).

Consider a process where the reactive power output from all WTGs is increased simultaneously. This could be achieved by a central controller sending every WTG a reactive power set-point Q_{set}. With $Q_{set} = 0$, none of the WTGs would be at their voltage limits, so all could respond to a change in the set-point ΔQ_{set}. The example system consists of 19 WTGs, so the total change in reactive power supplied to the collector bus would be approximately $19 \times \Delta Q_{set}$. (Losses would change by a small amount.) As Q_{set} increases, voltages across the collector system will increase, with the most dramatic increases occurring at the remote ends of radial feeders. Eventually those WTGs at the ends of feeders will encounter their upper voltage limits. To ensure the voltage limit is not exceeded, protection overrides the Q_{set} set-point. Reactive power output can no longer increase with increasing Q_{set}, and in fact may fall to ensure the voltage does not rise above the limit. As Q_{set} continues to increase, more and more WTGs will reach their upper voltage limits, preventing further increase in their reactive power output.

The process described above was simulated using a continuation power flow. Results of this process, for the example system of Figure 15, are presented in Figure 16. Each curve in the figure corresponds to a different, randomly chosen, set of active power generation values for the WTGs. It can be seen that the reactive power output saturates in every case. For small Q_{set}, the slope of each curve is close to 19, the number of WTGs. However, as Q_{set}

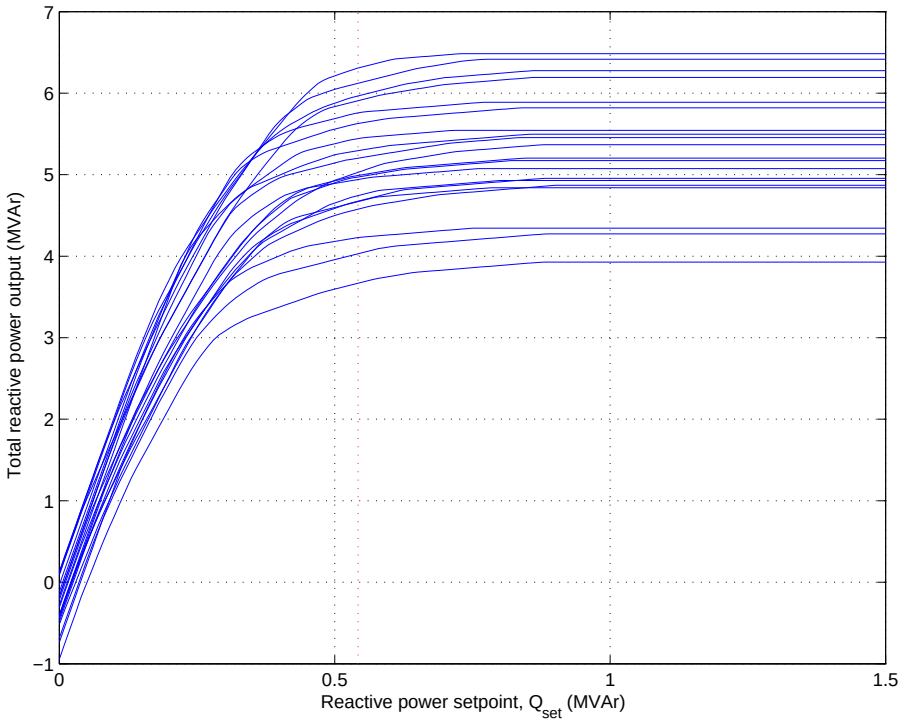

Figure 16: Variation of total reactive power with set-point Q_{set}.

increases, and WTGs progressively encounter their voltage limits, the slope steadily decreases. Eventually all WTGs are on voltage limits, and further increases in Q_{set} have no effect.

For this example, all WTGs are rated to produce 1.65 MW at 0.95 power factor (lagging and leading), which corresponds to maximum reactive power of 0.54 MVAr per turbine. This suggests the WTGs should be capable of supplying total reactive power of around $19 \times 0.54 = 10.3$ MVAr. In fact, based on Figure 16, the maximum available reactive power is actually less than 6.5 MVAr, and may be as low as 3.7 MVAr. The restriction is due to each WTG's upper voltage limit of $V_{max} = 1.1$ pu.

Wind-farms that include long radial feeders are most prone to saturation in total reactive power output. The effect is less significant for short feeders. Clearly, the collector system topology must be taken into account when assessing the total reactive power available from WTGs.

3.4 Transformer tap-changing gains

3.4.1 Background

It is not uncommon for step-up transformers associated with traditional generators to be used to regulate their high-side bus voltage. In a similar way, numerous wind-farms have sought to use the tap-changing capability of their collector transformers to regulate the voltage at the (high voltage) point of interconnection. It has been observed, though, that such tap changing may exhibit unstable behaviour, with the transformer tapping to an upper or lower limit and remaining there. Consequently, tapping-based voltage regulation is disabled in most wind-farms.

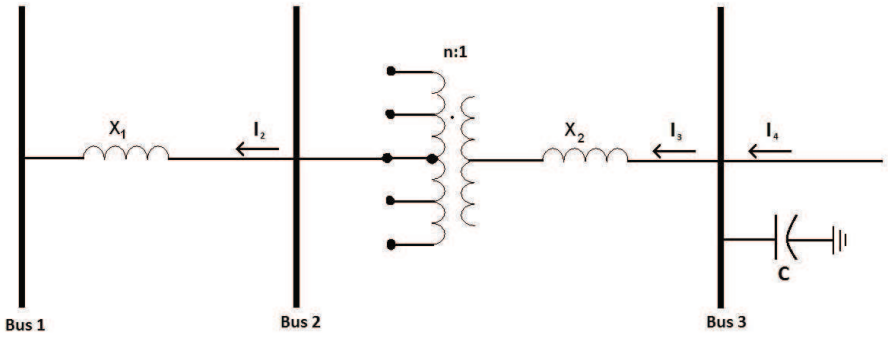

Figure 17: Power system for analyzing tap-changing dynamics.

In the following analysis, the simple power system of Figure 17 will be used to explore the nature of tap-changing instability, and to suggest sufficient conditions for ensuring stable behaviour. Given the tapping arrangement shown in Figure 17, the voltage regulator requires $\frac{dV_2}{dn} > 0$ for correct operation, i.e., it is assumed that an increase in tap raises the voltage on the high-voltage (tapped) side of the transformer. The following analysis shows that such a condition is not always satisfied.

3.4.2 Passive voltage support

Initially consider the case where the wind-farm has zero output, and the only device connected to the collector bus is a capacitor C. The injected current is given by

$$I_3 = -jBV_3$$

where $B = \omega C$ is the capacitive susceptance. Simple circuit analysis yields

$$V_2 = \frac{1}{1 - \frac{X_1 B}{n^2(1-BX_2)}} \times V_1. \tag{27}$$

In per unit, it is normal for $BX_2 \ll 1$. This allows (27) to be simplified, giving

$$V_2 = \frac{1}{1 - \frac{X_1 B}{n^2}} \times V_1. \tag{28}$$

Assuming constant susceptance B, differentiating gives

$$\frac{dV_2}{dn} = -\frac{2nX_1BV_1}{(n^2 - X_1B)^2}. \tag{29}$$

With capacitance connected to the collector bus, susceptance B is positive. It follows that $\frac{dV_2}{dn} < 0$, implying that tap changing is unstable. Capacitance is commonly connected to the collector bus to provide power factor correction and reactive support. Furthermore, when an SVC is at its capacitive limit, it is effectively just a capacitor.

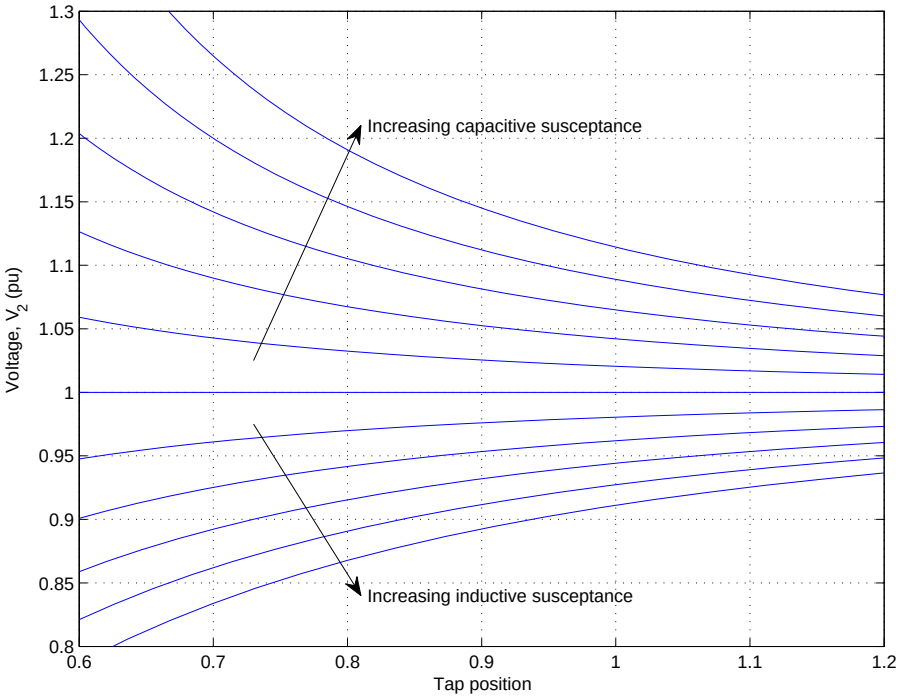

Figure 18: Curves of V_2 versus n for various values of capacitive and inductive susceptance.

Notice that if shunt reactors (inductors) are connected to the collector bus, then the susceptance becomes $B = -\frac{1}{\omega L}$. According to (29), $\frac{dV_2}{dn} > 0$ in this case. It follows that the tap changer would operate correctly to achieve voltage regulation. Figure 18 shows plots of V_2 versus tap position n for the system shown in Figure 17, with various levels of capacitive and inductive susceptance. The slopes of the curves are in agreement with (29).

The simplified analysis above assumed zero active power production from the WTGs. To explore this effect, active power of 1.0 pu, at unity power factor, was injected by the WTGs into the collector bus. The continuation power flow cases of Figure 18 were repeated with this power injection, and are shown in Figure 19. Notice that the conclusions drawn in the prior analysis remain true:

$$\begin{aligned} \text{capacitive susceptance} \quad &\Rightarrow \quad \frac{dV_2}{dn} < 0 \\ \text{inductive susceptance} \quad &\Rightarrow \quad \frac{dV_2}{dn} > 0. \end{aligned}$$

When STATCOMs encounter a limit, they act as a current source. It is therefore useful to consider the case of a reactive current source

$$I_3 = j\hat{I}_3 \tag{30}$$

injecting current into the collector bus. Note that $\hat{I}_3 > 0$ for an inductive source (reactive power delivered from the grid to the STATCOM), with $\hat{I}_3 < 0$ for a capacitive source (reactive power delivered from the STATCOM to the grid.) Again, simple circuit analysis yields

$$V_2 = V_1 - X_1 \frac{\hat{I}_3}{n} \tag{31}$$

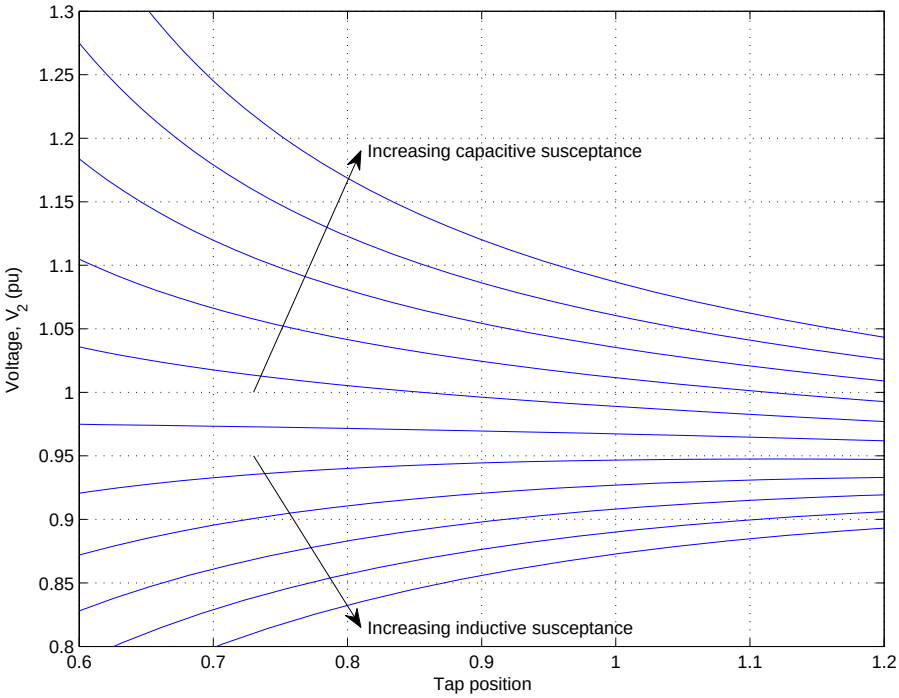

Figure 19: Curves of V_2 versus n taking into account WTG active power production.

and so

$$\frac{dV_2}{dn} = X_1 \frac{\hat{I}_3}{n^2}.$$

If the current source is inductive, $\frac{dV_2}{dn} > 0$ and hence tapping-based voltage regulation will operate correctly. However, if the current source is capacitive, $\frac{dV_2}{dn} < 0$, so tap-changer control will go unstable. The continuation power flows of Figure 18 were repeated for these current injection cases, with the results shown in Figure 20.

3.4.3 Active voltage support

Consider a reactive support device that injects voltage dependent current

$$I_3(V_3) = j\hat{I}_3(V_3)$$

into the collector bus. It can be shown that in this general case, $\frac{dV_2}{dn}$ takes the form

$$\frac{dV_2}{dn} = \frac{\hat{I}_3(V_3) + V_3 \frac{d\hat{I}_3(V_3)}{dV_3}}{\frac{n^2}{X_1} + \frac{d\hat{I}_3(V_3)}{dV_3}}. \tag{32}$$

In the special case where reactive support is provided by a capacitor,

$$\hat{I}_3(V_3) = -BV_3. \tag{33}$$

Substituting this into (32) and simplifying gives (29), as expected. The advantage of (32), though, is that more general forms of support may be considered.

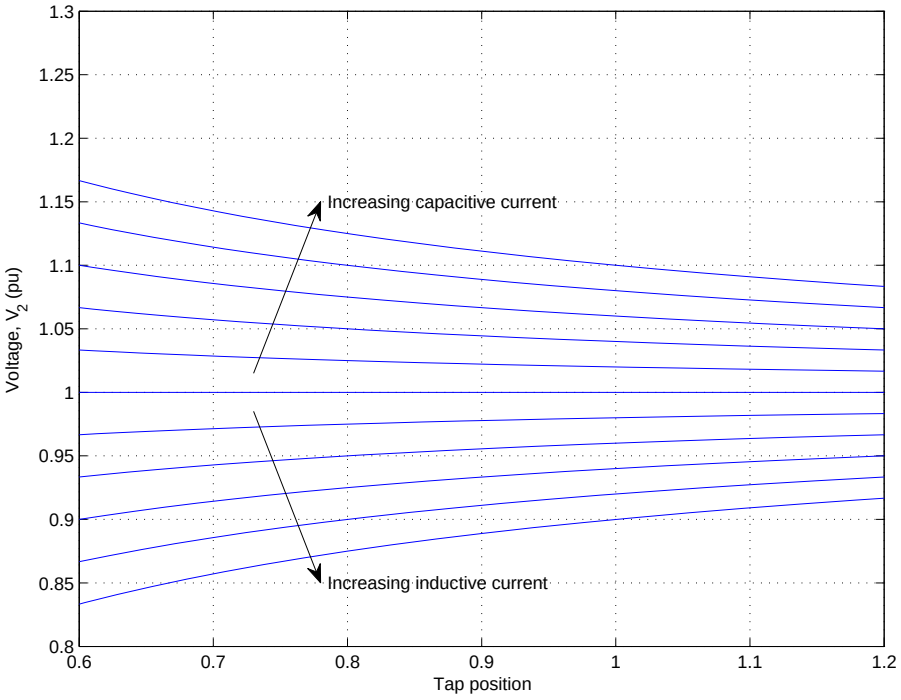

Figure 20: Curves of V_2 versus n for various values of capacitive and inductive current injection.

1) STATCOMs: Assume a STATCOM has current limits of $\pm\bar{I}_{stat}$. (Recall the current convention of Figure 17, which implies capacitive current is negative.) It is common for voltage control to employ a droop characteristic, such that the current injected into the collector bus is given by,

$$I_{stat} = \frac{\bar{I}_{stat}}{D_{stat}}\big(V - \bar{V}\big) \tag{34}$$

where D_{stat} is the droop value (typically around 0.03-0.05), $\bar{V}$ is the target voltage at zero output, and V is the collector bus voltage. This yields full output when the voltage difference exceeds the droop value. All quantities are in per unit.

With a fixed capacitor and a STATCOM at the collector bus, the total injected current is,

$$\hat{I}_3(V_3) = -BV_3 + \frac{\bar{I}_{stat}}{D_{stat}}\big(V_3 - \bar{V}\big), \tag{35}$$

and hence

$$\frac{d\hat{I}_3(V_3)}{dV_3} = -B + \frac{\bar{I}_{stat}}{D_{stat}}. \tag{36}$$

From (32), positive (stable) $\frac{dV_2}{dn}$ requires that

$$\hat{I}_3(V_3) + V_3\frac{d\hat{I}_3(V_3)}{dV_3} > 0. \tag{37}$$

Substituting (35) and (36) into (37) and simplifying gives

$$-2BV_3 + \frac{\bar{I}_{stat}}{D_{stat}}\big(2V_3 - \bar{V}\big) > 0.$$

Exploiting the fact that $V_3 \approx \bar{V}$ allows further simplification,

$$\frac{\bar{I}_{stat}}{D_{stat}} > 2B. \tag{38}$$

For a capacitor, $B > 0$, implying $D_{stat} > 0$. Therefore, $\frac{dV_2}{dn}$ will be positive if

$$0 < D_{stat} < \frac{\bar{I}_{stat}}{2B}. \tag{39}$$

It is interesting that the STATCOM droop characteristic must over-compensate the capacitor to ensure $\frac{dV_2}{dn} > 0$. To explore this result further, consider the situation if the droop characteristic only just compensated the fixed capacitor, i.e., $\frac{\bar{I}_{stat}}{D_{stat}} = B$. According to (35), the net current injection would be

$$\hat{I}_3(V_3) = -B\bar{V}, \tag{40}$$

which is effectively a constant capacitive current. It was shown in Figure 20, though, that $\frac{dV_2}{dn} < 0$ for such a current injection. By requiring the condition (38), the inductive effect of the droop characteristic overcomes the combined effects of the actual capacitor and the "apparent" capacitive current source (40).

2) SVCs: SVCs introduce a variable susceptance B into the current injection equation (33). With B functionally dependent upon V_3, the derivative $\frac{d\hat{I}_3}{dV_3}$ becomes,

$$\frac{d\hat{I}_3}{dV_3} = -B - V_3\frac{dB}{dV_3}. \tag{41}$$

Substituting (33) and (41) into (37) gives,

$$\begin{aligned} -BV_3 - V_3\big(B + V_3\frac{dB}{dV_3}\big) &> 0 \\ \Rightarrow \qquad 2B + V_3\frac{dB}{dV_3} &< 0 \\ \Rightarrow \qquad \frac{dB}{dV_3} &< -\frac{2B}{V_3}. \end{aligned} \tag{42}$$

Assume an SVC has symmetric susceptance limits $\pm\bar{B}_{svc}$, where capacitive susceptance is positive. A typical droop characteristic has the form

$$B_{svc} = \frac{\bar{B}_{svc}}{D_{svc}}\big(\bar{V} - V\big) \tag{43}$$

where parameters are defined similarly to (34), and are again in per unit. If a fixed capacitor with susceptance $-B_{fix}$ is connected to the collector bus together with the SVC, then the total susceptance is

$$B(V_3) = B_{fix} + B_{svc}(V_3),$$

and

$$\frac{dB(V_3)}{dV_3} = -\frac{\bar{B}_{svc}}{D_{svc}}.$$

It follows from (42) that $\frac{dV_2}{dn}$ is positive (stable) when

$$\frac{\bar{B}_{svc}}{D_{svc}} > \frac{2B}{V_3}.$$

To ensure this condition is satisfied over the full range of $B(V_3)$ requires that

$$\frac{\bar{B}_{svc}}{D_{svc}} > \frac{2(B_{fix} + \bar{B}_{svc})}{V_3},$$

or rewriting,

$$0 < D_{svc} < \frac{V_3 \bar{B}_{svc}}{2(B_{fix} + \bar{B}_{svc})}.$$

3.5 Transformer Tap-Changing Dynamics

This section addresses a similar issue to Section 3.4, but now considers the system dynamics rather than the steady-state condition. The results derived in Section 3.4 are "static" in that they do not depend on time or the previous states of the system. There are no functions of time or time derivatives.

Now consider the case where the tap-changing and voltage support controllers have their own dynamics. Specifically, the controllers for tap-changing and reactive support are single input single output (SISO) integral controllers that operate independently, as is typically the case when control is isolated on each particular piece of hardware.

The main consideration is the relative speed between the two control loops. It will be shown that if the tap-changing controller is sufficiently fast (aggressive) compared to the reactive support, instability may result.

Using the same system considered in Section 3.4 and shown in Figure 17, assume a reactive current injection into the collector bus as in (30). Voltage V_2 is given by (31) and V_3 is,

$$V_3 = \frac{V_1}{n} - X\frac{\hat{I}_3(V_3)}{n^2}. \tag{44}$$

Let target voltages (set by the operator) at bus 2 and 3 be $\bar{V}_2$ and $\bar{V}_3$. For simplicity, assume that continuous tap ratios are available. Then the independent SISO integral controllers for the tap ratio n and the reactive power injection $\hat{I}_3$ are,

$$\dot{n} = -k_n(V_2 - \bar{V}_2) \tag{45}$$

$$\dot{\hat{I}}_3 = (V_3 - \bar{V}_3). \tag{46}$$

Normally, the speed of each control loop would be scaled by some gain. In this case, the primary interest is stability and the important factor is the *relative* speed between the two loops. Therefore, the gains are normalized by the gain of the reactive support loop (46), leaving it with a gain of one. The gain k_n (positive) in (45) represents the relative speed of the two loops; increasing k_n means that tap changing is becoming faster and more aggressive relative to the reactive support.

To check the stability of the system, the dynamics are linearized about an equilibrium point. For simplicity, assume that the desired set-points are $\bar{V}_3 = 1$ p.u., and $\bar{V}_2$ is a function of the equilibrium tap ratio $\bar{n}$. This leaves $\bar{V}_2 = \bar{n}V_3$ (e.g. $\bar{n} = 1.05$). At this equilibrium

point, all derivatives will be zero and the system will remain there unless perturbed. Setting the derivatives (45) and (46) equal to zero, and substituting (31) and (44),

$$\dot{n} = 0 = -k_n(V_1 - X\frac{\hat{I}_3(V_3)}{n} - \bar{V}_2) \tag{47}$$

$$\dot{\hat{I}}_3 = 0 = (\frac{V_1}{n} - X\frac{\hat{I}_3(V_3)}{n^2} - \bar{V}_3). \tag{48}$$

An important distinction is the difference between a state (n or V_2) and the linearization point ($\bar{n}$ or $\bar{V}_2$). A fixed equilibrium point, denoted by a bar, is selected to conduct the linearization, but the system dynamics still evolve about that point.

Equations (47) and (48) are identical given the definition of $\bar{V}_2$ and may be solved for the equilibrium current injection,

$$\hat{I}_3(V_3) = -\frac{n(\bar{n}-1)V_1}{X} \tag{49}$$

completing the specification of the equilibrium point.

Taking the partial derivatives of (47) and (48), substituting (49) and assuming that $V_1 =$ 1 p.u. gives the linearized system dynamics,

$$\begin{bmatrix} \dot{n} \\ \dot{\hat{I}}_3 \end{bmatrix} = \frac{1}{\bar{n}^2}\begin{bmatrix} k_n\bar{n}(\bar{n}-1) & k_n\bar{n}X \\ 1-2\bar{n} & -X \end{bmatrix}\begin{bmatrix} \delta n \\ \delta\hat{I}_3 \end{bmatrix}, \tag{50}$$

which has a characteristic polynomial,

$$s^2 + s(-k_n\bar{n}(\bar{n}-1) + X) + \bar{n}^2 k_n X. \tag{51}$$

Given that the final term is positive by the definition of k_n, the s term must contain a positive coefficient to yield two stable eigenvalues. This condition holds when $0 < \bar{n} < 1$ for positive X. However, when $\bar{n} > 1$, there is a maximum tap changing gain k_n to ensure stability,

$$k_n < \frac{X}{\bar{n}(\bar{n}-1)}. \tag{52}$$

In short, if the bus 2 voltage set-point $\bar{V}_2$ is less than 1 p.u. ($\bar{n} < 1$) there is no stability issue. If that is not the case, however, then a sufficiently aggressive tap changer can cause the system to go unstable.

3.6 Supervisory Control of Reactive Power Support

As previously discussed, reactive power may be controlled by a combination of capacitors, tap-changing transformers and FACTS devices. The system operator desires to use this equipment in the most efficient way possible to meet requirements and often has multiple conflicting goals. For example, these goals may include minimizing capacitor switching, tap changing and power losses while maximizing reactive reserve. More sophisticated objectives are possible, like prioritizing different kinds of reactive reserve (i.e. capacitors versus STATCOMs) or maximizing the possibility of successfully dealing with a system fault. There is significant potential for better control performance by incorporating future knowledge, including wind and load forecasts.

This level of complexity suggests the need for a system-level control approach, where all the reactive power sources are controlled by a single controller. This approach may yield better performance than relying on the controls of the individual devices. This section focuses on longer-term supervisory control which makes decisions at a relatively slow rate, roughly once per minute or slower. Fault conditions or fast transients are assumed to be handled by standard control methods.

3.6.1 Problem Formulation

The proposed system-level control formulation can be treated as a dynamic optimization problem. An important aspect of this form of problem is the type of future information available, its quality, and the forecasting horizon. The goal here is to generate the best possible controller given the available information.

Consider an optimization problem with a finite horizon, even if very long, perhaps a year. The various types of future information can be grouped into five broad classes:

1. **Exact Future Knowledge -** Exact knowledge of the future for the full time horizon. This yields the maximum attainable performance, although it is unrealistic in practice. A less restrictive case assumes that exact future knowledge is available, but only for a short duration, e.g. a 24-hour exact forecast.

2. **Uncertain Future Knowledge -** Time-dependent future information with uncertainty of some type, including uncertain forecasts and time-dependent Markov transition probabilities. This information may be available for the full time horizon or a shorter duration.

3. **Cyclical Stochastic Knowledge -** General stochastic predictions about the future that are repetitive and cyclical. An example are Markov transition probabilities that change based on the time of day, but are repeated each day. This category is well-suited to model daily demand fluctuations as well as day/night wind patterns.

4. **Stationary Stochastic Knowledge -** Stationary stochastic predictions about the future, including Markov-chain based wind models. No explicit forecasting or time-dependent knowledge is required.

5. **No Explicit Future Knowledge -** Both optimization- and rule-based methods that do not explicitly account for the future.

Each of these five classes will generate controllers with different characteristics. Several controller subtypes are available for each class; the information class is identified for each controller type proposed in the following Section 3.6.2. The list is ordered roughly in decreasing order of complexity and performance. In general, having more information available does not guarantee improved performance, but it should do no worse than the baseline case. The two extreme cases (1 and 5) listed above may be undesirable, which forces the determination of the best tradeoff between performance and complexity. Specifically, the designer should determine the performance improvement available with increasing controller complexity in order to make an informed decision

1) Overall Optimization Strategy: The most general formulation describes the system dynamics using a function of the system state x, control input u, and disturbance w,

$$x_{k+1} = f_k(x_k, u_k, w_k). \tag{53}$$

The function f may or may not change with time, as represented by f_k.

For a given time series of states $(x_1...x_T)$, controls $(u_1...u_T)$, and disturbances $(w_1...w_T)$, a performance metric J is assigned to represent the total cost. A general optimization formulation represents this cost as a function Φ of the states, controls, and disturbances over a time window T,

$$J = \Phi(x_1...x_T, u_1...u_T, w_1...w_T). \tag{54}$$

Other formulations are available that generate a finite cost even with infinite stopping time, for example by discounting future costs.

Many different techniques are available to solve these types of problems, but optimal solutions can be difficult to obtain because the number of possible control sequences grows exponentially with time. If the total cost is restricted to be an additive cost function $c_k(x_k, u_k)$ that can be evaluated at each individual time-step,

$$\sum_{0}^{T} c_k(x_k, u_k), \tag{55}$$

techniques are available to drastically reduce computational requirements. The subscript k indicates that the cost may be a function of time. By focusing on problems of this type, the optimization problem may be stated formally as minimizing (55) subject to possibly time-dependent constraints $g_k(x_k, u_k)$,

$$\begin{aligned} &\min \sum_{0}^{T} c_k(x_k, u_k) \\ &\text{such that} \quad g_k(x_k, u_k) \leq 0 \quad \forall k. \end{aligned} \tag{56}$$

Controller performance was evaluated by generating test optimization-based controllers for three cases, including the two extreme cases: exact future knowledge, stationary stochastic knowledge, and no explicit future knowledge. In addition, these three controllers are compared to a "baseline" algorithm that uses hysteresis-based switching of the capacitors based on current reactive power demand.

2) Example System: The various control techniques can be illustrated using a simple test system. This system consists of a wind-farm collector network connected to an infinite bus through a substation. The substation uses four capacitor banks and a STATCOM for reactive power compensation, as shown in Figure 14. The optimization goal is to minimize both STATCOM usage and capacitor switching. The STATCOM is assumed to perfectly regulate the bus voltage V_3 and supply any reactive power not supplied by the capacitors. For now, the STATCOM is also assumed to have unlimited capability, but realistic limits may be easily implemented. This yields a relatively simple power flow problem, while clearly illustrating the control design tradeoffs. The power flow equations are solved to determine the reactive power required to hold the bus voltage at 1 p.u., and the optimization is simply the distribution of this reactive power between the STATCOM and capacitors.

To model this system in terms of (56), the system has four states x representing the current state of each capacitor bank, either on or off. Four controls u represent the command to turn each capacitor bank on or off. Thus the system dynamics (53) reflect the simple result that at the next time-step, the capacitor state x_{k+1} will match the current command u_k.

For the cost function, the number of capacitor switches N_{CS} is weighted by a penalty α to reflect maintenance and wear costs. The STATCOM usage $\bar{S}$ is calculated based on the current reactive power demand and the capacitance established by the control u_k. It is defined as the time integral of STATCOM output over the time-step. Of interest is the relative tradeoff between capacitor switches and STATCOM usage, so only one tuning parameter is needed. Accordingly, the stage cost has the form,

$$c_k(x_k, u_k) = \alpha N_{CS} + abs(\bar{S}). \tag{57}$$

The definitions of $c_k(x, u)$ and $f_k(x, u)$ form the basic optimization problem and are used in the various algorithms that follow.

3.6.2 Control Design Methods for Various Information Classes

The control design methods proposed here are standard techniques. The main ideas are presented here, but full details are available in standard texts [36, 37].

1) Deterministic Dynamic Programming: In the case of exact future knowledge, Deterministic Dynamic Programming (DDP) can be used to solve (56). For each time-step, the optimal "cost to go" function $J_k^*(x)$ is calculated. It represents the minimum cost required to go from time k and state x to the final time T. Starting at the final time T, the terminal cost (if any) is assigned for the final state, yielding $J_T^*(x)$. The algorithm proceeds by backward recursion,

$$J_k^*(x) = \min_{u \in U}[c_k(x, u) + J_{k+1}^*(f_k(x_k, u))], \tag{58}$$

where $c(x, u)$ is the instantaneous cost as a function of state and control. Recall that the function $f_k(x_k, u_k)$ determines the next state x_{k+1}. This equation (58) represents a compromise between minimizing the current cost $c_k(x, u)$ and the future cost $J(x_{k+1})$. This formulation is entirely deterministic with no stochastic disturbances because the exact future is known. Anything that changes with time, e.g. reactive power demand, is included in the time-varying cost $c_k(x, u)$ or dynamics $f_k(x_k, u_k)$. In this case, the cost is given by (57) and changes based on the required reactive power.

The optimal control u^* is any control that achieves the minimum cost $J_k^*(x)$ in (58),

$$u_k^*(x) = \operatorname*{argmin}_{u \in U}[c(x_k, u) + J_k^*(f_k(x_k, u))]. \tag{59}$$

This method requires two steps: an off-line step to calculate the controller using the future knowledge, and an on-line step where the control is causally implemented, possibly in real-time. The off-line step solves (58), and the end result is a control policy $u_k^*(x)$ and a cost-to-go $J_k(x)$, both for all times k. In the on-line implementation, one may either use the policy $u_k^*(x)$ or calculate the control on-line using (59) and the cost-to-go $J_k(x)$. Intuitively, $J_k(x)$ represents the minimum cost required to operate from time k until time T when starting in state x. It essentially contains the future information about the system.

2) Stochastic Dynamic Programming: Stochastic Dynamic Programming (SDP) is used to incorporate uncertain future knowledge, stationary stochastic knowledge in this case. This algorithm is a variant of the deterministic version described previously, but the main ideas are the same. The key difference is that the future is uncertain, so everything is based on an expectation of the future E_w over the disturbance w. While the designer still wished to solve (56), the algorithm can no longer solve it exactly due to the uncertain future. Instead, the algorithm uses a slightly different optimization formulation,

$$\begin{aligned} &\min\ E_w \sum_{0}^{\infty} \gamma^k c_k(x_k, u_k) \\ &\text{such that} \quad g_k(x_k, u_k) \leq 0 \quad \forall k. \end{aligned} \tag{60}$$

This formulation differs from (56) in several ways. The future cost is discounted by the factor $\gamma < 1$, which keeps the sum finite. This technique is called "infinite horizon discounted future cost." Although the time horizon is no longer finite, a value of γ close to one forces the algorithm to consider a "reasonable" time horizon, while discounting the infinite future.

To use the algorithm,

$$V^*(x) = \min_{u \in U} E_w[c(x,u) + V^*(f(x,u,w))] \tag{61}$$

is solved for the "Value Function" $V(x)$. The value function is very similar to the cost-to-go $J_k(x)$ in (58). The primary difference is that $V(x)$ is not a function of time, only of the state. It represents the expected future cost of being in state x. The time horizon is infinite, and hence $V(x)$ does not change with k. The optimal control u^* is again any control that achieves the minimum cost $V^*(x)$ in (61),

$$u^*(x) = \operatorname*{argmin}_{u \in U} E_w[c(x,u) + V^*(f(x,u,w))]. \tag{62}$$

The control policy is also independent of time and hence is a stationary policy.

The future disturbances, wind power in this case, are specified via a finite-state Markov chain rather than exact future knowledge. This wind model adds additional states to the model. In general, the designer must determine the probability distribution of the disturbance w based on the current state and control,

$$P(w_k | x_k, u_k). \tag{63}$$

A one-state Markov chain has been used for these investigations. The current wind power P_k is the state. The probability of the wind power at the next time-step depends on the current wind power, which means estimating the function

$$P(P_{k+1} | P_k). \tag{64}$$

The designer may choose how this disturbance is specified. For example, the disturbance may be the value of the wind power at the next time-step, or it may be given as the change in wind power. More complex models can be used by adding additional model states, for example the last three recorded values of the wind power.

The transition probabilities (64) can be estimated from known wind patterns. The powers P are discretized to form a grid. For each discrete state P_k there are a variety of outcomes P_{k+1}. The probability of each outcome P_{k+1} is estimated based on its frequency of occurrence, and is a function of the current wind power.

3) Instantaneous Optimization: The simplest optimization-based algorithm seeks to minimize cost with no future knowledge. This technique is termed Instantaneous Optimization (IO) because it has no estimate or prediction of the future and the control is generated by minimizing the current cost at each instant,

$$u^*(x) = \underset{u \in U}{\operatorname{argmin}}\, c(x, u). \tag{65}$$

The control decision clearly lacks the future estimates of (59) and (62).

4) Baseline Controller: The baseline controller is not based on optimization at all, but a simple rule-based hysteresis strategy. Recall that the STATCOM usage $\bar{S}$ is the difference between the required reactive power and that supplied by the capacitors. A switching threshold β is assigned, and when the STATCOM usage exceeds this threshold, an additional capacitor bank is switched in or out. Define NC as the number of capacitor banks currently switched in. Then the update rule can be written as,

$$NC_{k+1} = \begin{cases} NC_k + 1 & \text{if } \bar{S} > \beta \\ NC_k - 1 & \text{if } \bar{S} < -\beta \\ NC_k & \text{otherwise.} \end{cases} \tag{66}$$

3.6.3 Simulation Results

The various types of controllers discussed in Section 3.6.2 were designed and tested using the example system to evaluate their effectiveness. Wind data from the National Renewable Energy Lab's EWITS study was used. The simulation covered a 30-day period, and the controller commands updated every 5 minutes. Each controller was designed with the appropriate level of information: controllers that use exact future knowledge were given the entire wind-power trace ahead of time, stochastic controllers were given the probability distribution (64) for the test period, and the other two controllers were not given any future information.

For each controller type, a number of different controllers were designed with varying values of the penalty α in (57) or the hysteresis threshold β in (66). This yielded a range of controllers of the same type with varying attributes. The results are shown in Figure 21. The horizontal axis shows the number of capacitor switches. The vertical axis represents total STATCOM usage, measured as cumulative absolute value $\sum abs(\bar{S})$. As the optimization goal is to minimize both capacitor switching and STATCOM usage, the best performance is found in the lower left of the plot.

3.6.4 Discussion

The DDP controllers designed with perfect information demonstrate the best performance, which is to be expected. Perhaps more surprising is that the other three controller types all generate similar performance. This motivates an open research question: What level of future information is appropriate? For the five information classes enumerated in Section 3.6.1, the two simplest cases (classes 4 and 5) yield similar performance, but the most complex case (class 1) yields vast improvements. This points to a "middle ground" of controller complexity, where significant improvements may be found with reasonably complex controllers of classes 2 to 4. If exact future knowledge provided no benefit, simple controllers could be used while attaining optimal performance.

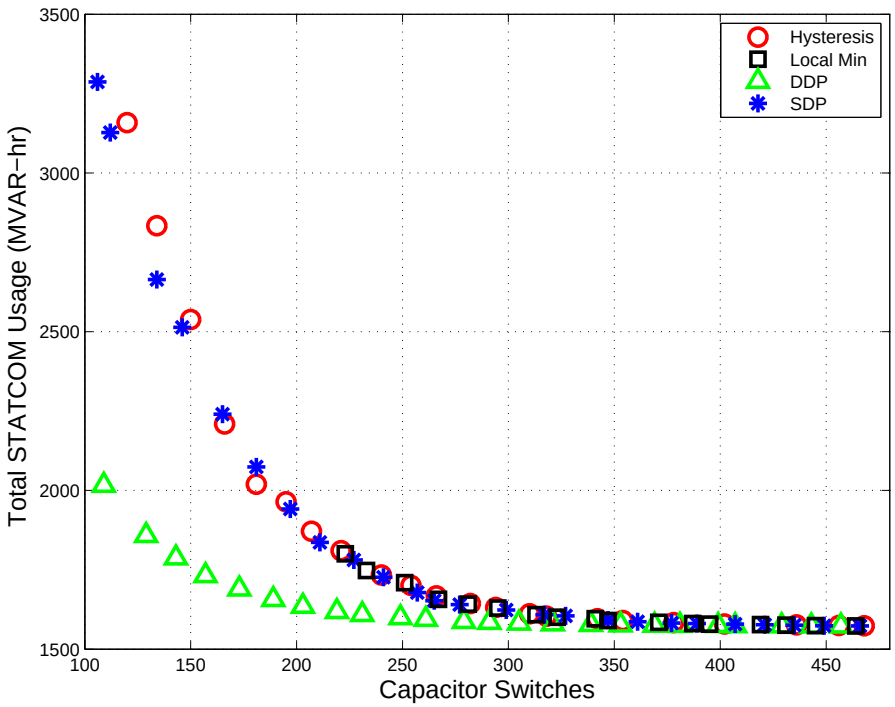

Figure 21: Performance of various types of optimal controllers based on different types of information. Best performance is attained with low STATCOM usage and low capacitor switching, in the bottom left of the figure. These data are for one month periods. Detailed time traces are shown in Figure 22.

The IO controllers generate identical performance to the baseline hysteresis method because they essentially do the same task. With no future knowledge, the instantaneous optimization is based solely on the cost function (57). A capacitor switch will not occur until the STATCOM usage exceeds the cost of the capacitor switch, which acts as a threshold policy. Arguably, the simple hysteresis method is a rudimentary optimization.

The behaviour of the instantaneous optimization has a discontinuity, as shown by the unpopulated region for lower capacitor switches. At each time-step, the STATCOM usage is evaluated for only that time-step. The maximum savings obtained by switching in one capacitor bank is finite, specifically the value of the capacitor bank times the time-step. If the cost of a capacitor switch exceeds this maximum, no capacitors will ever be switched on because the decrease in STATCOM usage is always less than the cost of a capacitor switch.

The performance of the SDP stochastic controllers is identical to that of the simpler controllers without any future knowledge. This implies that the Markov chain wind model does not provide any additional future information. This is clear from the calculated statistics (64) as the distribution of change in wind power is approximately constant regardless of the current wind power. The SDP controllers studied here use a very simple Markov chain wind model. More sophisticated controllers can be designed that use additional states and generate better performance, for example by storing the last few wind-power values rather than just the current value. They will still be classified as having stationary stochastic knowledge (class 4). However, independent work [38] suggests that Markov chains are not particularly good

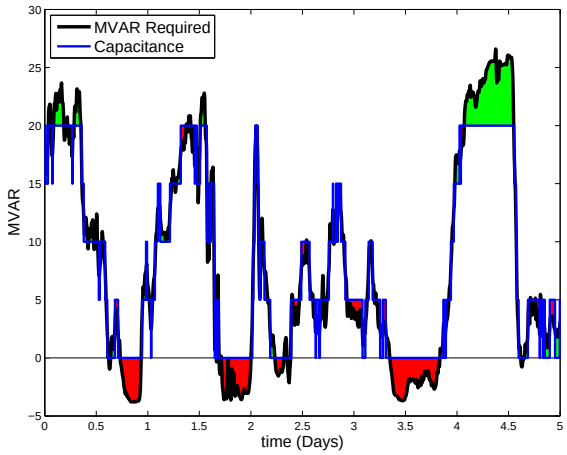

(a) Minimum STATCOM/max switching case for Deterministic Dynamic Programming with exact future knowledge.

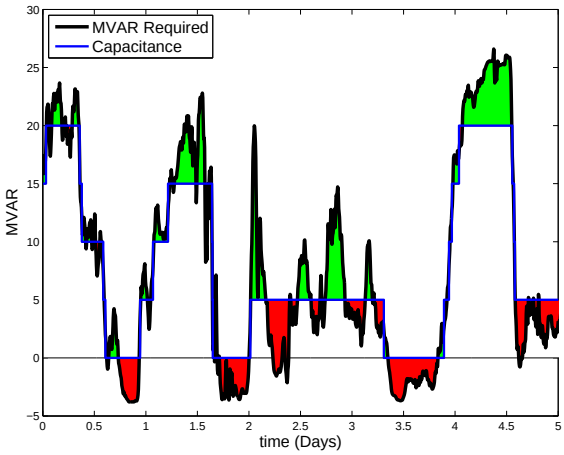

(b) Moderate switching (98 Switches) with Deterministic Dynamic Programming and exact future knowledge.

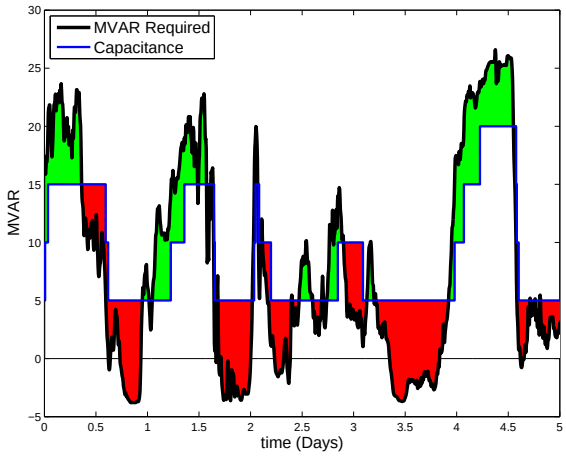

(c) Moderate switching (98 Switches) with Stochastic Dynamic Programming and future statistics.

Figure 22: Time traces of wind-farm reactive power control. The solid black line is the required reactive power. The solid blue line is the capacitance, which changes in discrete steps. The green and red regions represent the positive and negative STATCOM usage required to exactly meet the reactive power demand.

at wind forecasting.

Although the example system used here is very simple, the optimization framework of Section 3.6.1 can handle quite complex systems. Additional attributes [39] may be considered, including reserve requirements, failure probabilities, short and long term STATCOM limits, and capacitor discharge times. The downside of this framework is computation, which typically grows exponentially with the number of system states. Including all the equipment in a substation is feasible, but including all the equipment in a region is probably not. These techniques can provide the most benefit for systems with complex dynamics, constraints, non-intuitive behaviour, and a relatively small number of actuators (<15). Large problems can

often be partitioned [40, 41] with some loss of optimality, i.e. solving for the reactive power output of each substation, then solving for the reactive power supply within each substation to meet that requirement.

3.7 Conclusions

The control of reactive power support for wind generation is a challenging problem on several levels. WTGs themselves may be used to provide reactive power support, but the design of the collector network may limit their reactive power output. This has been illustrated using an accurate model of a real wind-farm.

It has been shown that wind-farm voltage regulating schemes are susceptible to instability. Two instability mechanisms were explored, with the analysis highlighting the difficulty of coordinating multiple types of equipment with independent SISO controllers. It was shown that capacitive susceptance could cause a reversal of the tap-changing transformer voltage gain, with the high-side voltage decreasing (instead of increasing) with increasing tap ratio. In such cases, transformers will tap to their high or low limit and remain there. Furthermore, under certain conditions, interactions between the controllers of tap-changing transformers and reactive current sources, such as STATCOMs, can lead to instability.

Higher-level scheduling of reactive support devices within a wind-farm should take into account competing objectives, such as minimizing capacitor switching whilst maximizing the dynamic response capability of STATCOMs/SVCs. The stochastic nature of wind makes this a challenging problem though. A variety of control strategies have been considered, with varying assumptions about future information: some required perfect prediction, some used stochastic predictions, and some had no information. The results demonstrated that future knowledge plays a vitally important role in determining optimal solutions. In contrast, rudimentary future knowledge, in the form of simple wind forecasts based on Markov chains, provides negligible benefit. This leaves an open research question regarding the role of forecasting in these systems, and the relative tradeoff between controller complexity and performance as more information becomes available.

4 Impact of Wind Power Variability on Sub-transmission Networks

4.1 Introduction

It is often convenient and economical to connect distributed generation, in particular wind-farms, at sub-transmission levels (40-120 kV). In fact, in many cases it is unavoidable as only a lower voltage network is available. However, relative weakness of the sub-transmission network, characterized by low short-circuit ratios and high impedances [42], poses serious challenges for the large-scale integration of variable generation. In the case of wind power, its inherent variability can lead to unusual reactive power absorption and injection patterns. Since reactive power is closely coupled with voltage magnitudes and voltage regulating assets, wind-power variations at multiple nodes may affect bus voltages and transformer tap positions in complicated and unexpected ways.

Many utilities require wind-farm operators to regulate the voltage at the point of interconnection (POI) to a set-point value determined by the system operator. Nevertheless, varying power flow can cause voltage fluctuation at unregulated load buses that are sometimes located far from the POI. As voltage fluctuations can be problematic for consumers, utilities are required to install additional voltage regulating equipment. Varying power flow can also result in a higher frequency of tap-changing operation of transformers that connect weak sub-transmission networks to the transmission system. This increase is unacceptable for asset owners as it may significantly shorten the lifetime of these expensive devices.

Therefore it is important to examine interactions between wind-farm voltage regulation and other, pre-existing voltage regulating equipment, such as tap-changing transformers, and coordinate their goals to achieve optimal operation of the grid. Previous studies have shown for radial distribution feeders that voltage regulation at the POI tends to increase tap-changing operations [43]. However, many sub-transmission and distribution networks have a mesh structure. The presence of multiple wind injection nodes in a mesh network further complicates the impact of wind on voltages and taps. Existing techniques for analyzing power system response provide limited insights into the complex interactions between regulating devices and variable generation.

This chapter examines the impact of wind generation on sub-transmission networks, focusing particularly on the effect of power flow variability on the voltage profile and transformer tap-changing. Studies are based on a mesh network that serves the south-eastern region of Michigan. It is anticipated that major wind developments will occur in this region, and that the wind-farms will be connected to the 40 kV sub-transmission network. Sensitivity analysis, based on the power flow Jacobian, has been used to identify transformers that are most sensitive to wind-power variability at two sub-transmission wind generation nodes. Power flow continuation methods are also used to produce contour diagrams that allow more extensive investigations of the quantities that are most sensitive to wind injections at these two nodes.

The use of the power flow Jacobian for sensitivity analysis is not new, with applications dating back to the late 1960s [44]. Since then, sensitivity analysis has been applied in a wide range of power system studies, from voltage stability [45, 46, 47] to assessing the impact of distributed generation on line losses [48]. Continuation methods have been in existence for many years [49], and first found application in power system studies in the early 1980s, see for example [50]. Subsequent power system applications of continuation methods include voltage stability studies [51] and solution space investigations [52]. The chapter considers the use of

these methods to examine the impact of active power injection on tap positions and voltage magnitudes in the context of wind power.

The chapter is structured as follows. Section 4.2 describes analysis tools used to investigate the impact of wind injection. Section 4.3 applies these tools to the network of interest, explains various observed patterns, and establishes general trends in voltage regulation and tap-changer operation in weak sub-transmission systems. The temporal characteristics of tap-changer operation are discussed in Section 4.4, and line congestion is considered in Section 4.5. Conclusions are provided in Section 4.6.

4.2 Power System Analysis Tools

4.2.1 Sensitivity Analysis

The power flow is fundamental to power system analysis, underpinning studies from contingency analysis to system planning. The power flow problem consists of a set of nonlinear algebraic equations that can be expressed as,

$$P(\theta, V) = 0 \tag{67}$$

$$Q(\theta, V) = 0 \tag{68}$$

where (67) describes the active power balance at PV and PQ buses, (68) describes the reactive power balance at PQ buses, θ is the vector of voltage angles (relative to the slack bus) at all PV and PQ buses, and V is the vector of voltage magnitudes at PQ buses [53]. It follows that P and θ have the same dimensions, and likewise the dimensions of Q and V are equal.

Transformer taps can be incorporated into the power flow equations by assuming tap positions a_i are continuous variables, and noting that each transformer regulates a particular bus voltage. That bus voltage magnitude V_i takes on a known fixed value, and so it can be replaced in (67)-(68) by the new variable a_i. The power flow equations can be generalized accordingly by replacing the voltage vector V with $\mathcal{V} = \begin{bmatrix} \tilde{V} \\ a \end{bmatrix}$ where $\tilde{V}$ is the vector of voltage magnitudes at non-regulated buses, and a is the vector of tap positions associated with the transformers that are regulating bus voltages. Note that Q and $\mathcal{V}$ still have equal dimensions.

Taking partial derivatives of P and Q with respect to θ and $\mathcal{V}$ gives the linearized relationship,

$$\begin{bmatrix} \Delta P \\ \Delta Q \end{bmatrix} = \begin{bmatrix} P_\theta & P_\mathcal{V} \\ Q_\theta & Q_\mathcal{V} \end{bmatrix} \begin{bmatrix} \Delta\theta \\ \Delta\mathcal{V} \end{bmatrix} \tag{69}$$

where $P_\theta \equiv \frac{\partial P}{\partial \theta}$, and likewise for the other sub-matrices. Of interest is the way in which variations ΔP in the injected active power at wind-farm locations affect voltage magnitudes and tap positions, which are given by $\Delta\mathcal{V} = \begin{bmatrix} \Delta\tilde{V} \\ \Delta a \end{bmatrix}$. For transmission systems, where resistance is negligible, the off-diagonal blocks in (69) are almost zero, and so are normally neglected. This decouples ΔP from $\Delta\mathcal{V}$. However in sub-transmission and distribution networks, where resistance is non-negligible, the off-diagonal blocks become important. To understand how $\Delta\mathcal{V}$ varies with ΔP, the Matrix Inversion Lemma [54] can be used to give,

$$\begin{aligned} \Delta\mathcal{V} = &- \left[Q_\mathcal{V} - Q_\theta P_\theta^{-1} P_\mathcal{V}\right]^{-1} Q_\theta P_\theta^{-1} \Delta P \\ &+ \left[Q_\mathcal{V} - Q_\theta P_\theta^{-1} P_\mathcal{V}\right]^{-1} \Delta Q. \end{aligned} \tag{70}$$

Assuming that reactive power remains unchanged at PQ buses, so $\Delta Q = 0$, it follows that the desired sensitivities are given by,

$$\begin{aligned}\Delta\mathcal{V} &= -\left[Q_{\mathcal{V}} - Q_\theta P_\theta^{-1} P_{\mathcal{V}}\right]^{-1} Q_\theta P_\theta^{-1} \Delta P \\ &= S_{\mathcal{V}}\, \Delta P \end{aligned} \tag{71}$$

where $S_{\mathcal{V}} = \begin{bmatrix} S_{\tilde{V}} \\ S_a \end{bmatrix}$, and

$$\begin{aligned} \Delta\tilde{V} &= S_{\tilde{V}} \Delta P \quad \text{for buses where voltages are not regulated,} \\ \Delta a &= S_a \Delta P \quad \text{for transformer taps.} \end{aligned}$$

Later analysis will also make use of,

$$\begin{aligned}\Delta\theta &= \left[P_\theta - P_{\mathcal{V}} Q_{\mathcal{V}}^{-1} Q_\theta\right]^{-1} \Delta P \\ &= S_\theta\, \Delta P. \end{aligned} \tag{72}$$

4.2.2 Continuation Power Flow

Sensitivity values only provide local information around a single operating point. This can be helpful in identifying bus voltages and transformer taps that are highly sensitive to wind injection at a certain operating point. However sensitivity analysis may not accurately capture the behaviour of these variables in response to large changes in the system.

The power flow equations (67)-(68) can be written in generalized form as $f(x) = 0$, where f and x have the same dimension. This problem is fully determined, so solutions will be points. If a single parameter is allowed to vary, for example the active power at a PV or PQ bus, or the voltage set-point at a voltage regulated bus, the problem takes the form,

$$f(x, \lambda) = 0, \tag{73}$$

where λ is the single free parameter. Now the problem has one more variable than constraint, so is under-determined. In this case, the solution is no longer a single point, but rather defines a curve. Freeing a second parameter results in a surface which can be shown as a collection of curves, i.e. contour diagram, similar to a topographic map with contours of elevation. This concept underlies the continuation power flow.

Continuation methods for solving problems of the form (73) are well documented [49, 55]. Predictor-corrector algorithms, such as the Euler homotopy method, provide a robust process for obtaining a sequence of points along the desired curve. Applications of this particular method to power system problems are discussed in [50, 52].

The continuation power flow enables a range of studies that assist in assessing the impact of wind power in weak grids, including:

1. Exploring parametric influences in the relationship between wind power injection and bus voltages, tap positions and line flows, and

2. Extending those studies to consider interactions between multiple wind-injection points.

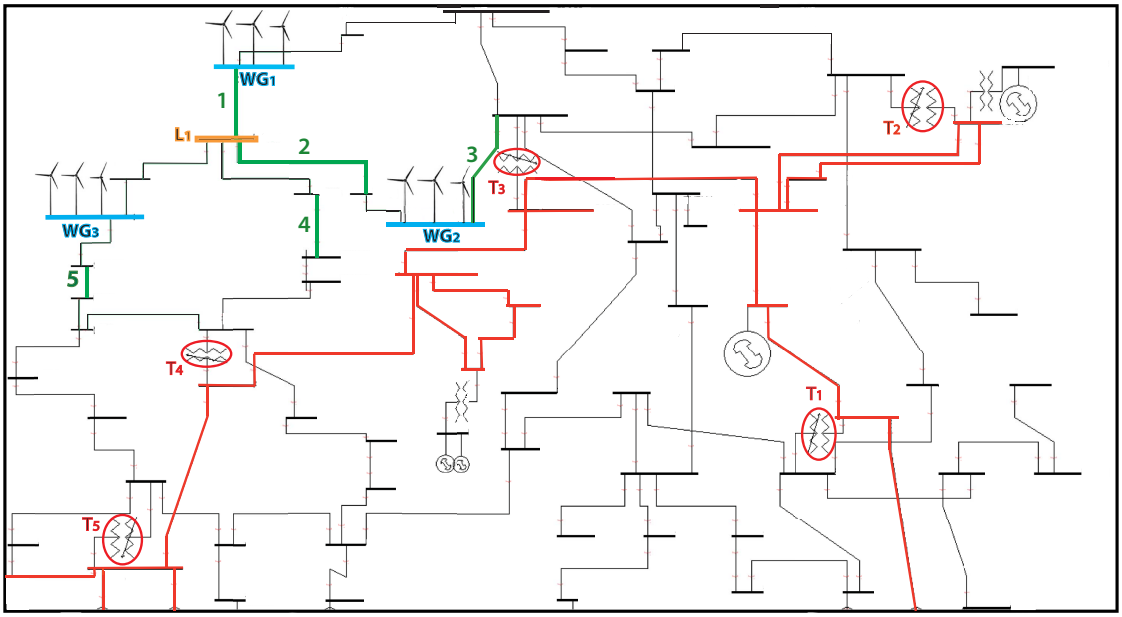

Figure 23: Wind development network: wind-injection nodes (blue), load bus L_1 (orange), the 120 kV transmission system and the 120/40 kV tap-changing transformers (red), the 40 kV sub-transmission network (black). Lines of interest in later congestion studies are shown in green.

4.3 Grid Analysis

Figure 23 shows a section of an actual power grid that is being studied for wind development. Active power is delivered from central power plants to the 40 kV sub-transmission system through a 120 kV transmission loop that is highlighted in red. At the interconnection points, the lower voltage (40 kV side) is regulated by five tap changing transformers highlighted by red ellipses. Initial studies consider wind-injection nodes WG_1 and WG_2, highlighted in blue, each with a capacity 50 MW. The third wind-farm WG_3 will be introduced in Section 4.5. Typically distribution companies require wind-farm operators to regulate the voltage at the point of interconnection to its set-point value, and this makes reactive power compensation at the wind-injection nodes indispensable.

To better understand the impact of this local reactive compensation on transformer tap operation and voltage magnitudes of adjacent nodes, this section and the following will contrast two cases:

1. No compensation at wind-injection nodes.

2. Compensation of ± 15 MVAr at each wind-injection node.

The case of no compensation is often not permitted by the system operator as voltage fluctuations caused by wind variability place enormous stress on voltage regulating equipment in distribution substations. Figure 24(a) shows the voltage contour diagram of load bus L_1 (highlighted in orange in Figure 23) which is in the vicinity of the wind-injection nodes. The region of interest, corresponding to the feasible range of wind injection at each node, is highlighted in the red box, and an enlarged version is shown in Figure 24(b). As wind

injection at the nodes simultaneously varies from 0 to 50 MW, voltage increases from 0.99 p.u. to 1.10 p.u. This voltage rise phenomenon, caused by wind-power injection on weak networks [56], has led to stricter grid standards requiring large distributed-generation installations to operate in voltage control mode. Figure 25 shows voltage contours of the same bus for the case of ± 15 MVAr compensation and, as shown in Figure 25(b), the voltage fluctuation range is now reduced to 0.99-1.05 p.u. However later studies illustrate that even though the no-compensation case may appear extreme and impractical, it is useful in the way it highlights the need for coordination between reactive compensation at wind-injection nodes and transformer tap operation.

The transformer tap sensitivity values for the two cases mentioned above are presented in Tables 1 and 2 respectively. Three operating points were considered, namely no wind, 40% and 80% wind output, and 100% correlation between wind injections was assumed. The latter two operating points correspond to medium and high wind generation respectively. It can be noticed that tap positions are in general more sensitive to wind injection in the case of ± 15 MVAr reactive compensation and that T_3 has the highest sensitivity values followed by T_4 and T_5. Furthermore, in the case of ± 15 MVAr reactive compensation, tap sensitivity is high at no wind, peaks at medium wind and drops to its lowest at high wind. This pattern is most visible for T_3 and T_4. In contrast, the no-compensation sensitivity values are highest at no wind and are almost zero at medium and high wind.

These sensitivity values provide an indication as to which transformers and buses are most sensitive and at what range of wind injection. With that knowledge, contour diagrams of relevant variables (tap positions or voltage magnitudes) can be generated. Figure 26(a) shows the tap position contour diagram of T_3 which overall had the highest sensitivity values. By looking at the region of interest shown in Figure 26(b), we see that at low to medium wind injection, tap contour lines (each corresponding to a tap step) are closely spaced whereas at higher wind the tap position does not change at all. Contrasting Figures 25(b) and 26(b) reveals an interesting pattern. Regions of high tap and low voltage sensitivity almost entirely overlap.

Moreover there are discontinuities in the contour lines when injection is high at one node and low at the other. These somewhat symmetrical discontinuity points correspond to limits of reactive compensation at each injection node. As wind injection increases, reactive compensation absorbs more reactive power until its inductive limit is encountered. As wind injection continues to increase, the voltage magnitude of the injection node and adjacent nodes starts to rise. Figures 27 and 28 show the contour lines corresponding to inductive limits of WG_1 and WG_2 superimposed on voltage magnitude and tap position diagrams respectively. The solution space is divided into four regions labelled A, B, C and D. In region A, both WG_1 and WG_2 are regulating. In region C, WG_2 has reached its inductive limit but WG_1 is still regulating, whereas in region D the situation is the reverse. In region B both WG_1 and WG_2 have reached their inductive limits. This latter region corresponds with where T_3 tap position stabilizes. According to the sensitivity values, this is also the case for all other transformers. The tap position contour diagram of T_3 for the case with no compensation, shown in Figure 29, also confirms, albeit in a negative way, the observation that reactive compensation results in higher tap sensitivity. Therefore, in the absence of any voltage regulation at the injection nodes, tap position sensitivity is reduced.

However, before concluding that there exists a tradeoff between voltage regulation at the injection nodes and tap change operation, the actual tap-changing operation of transformers under normal operating conditions, prior to wind, should be investigated. This base case,

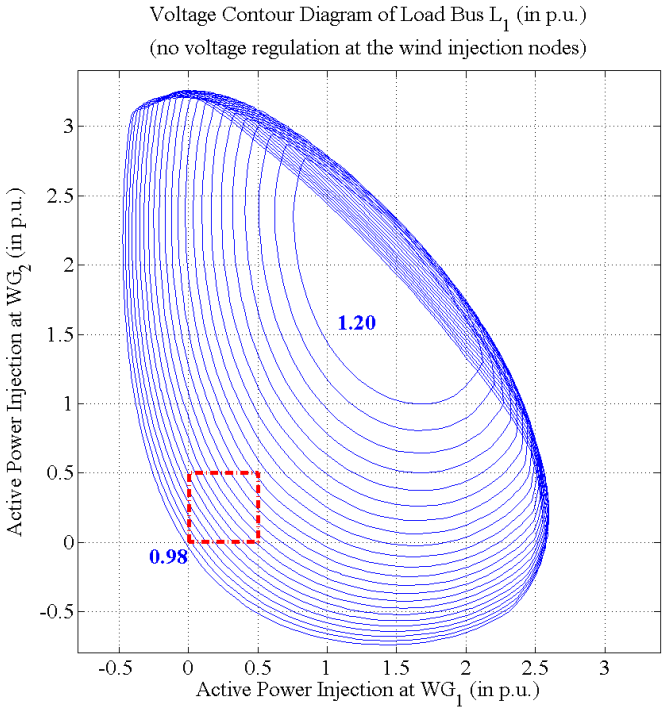

(a) Global

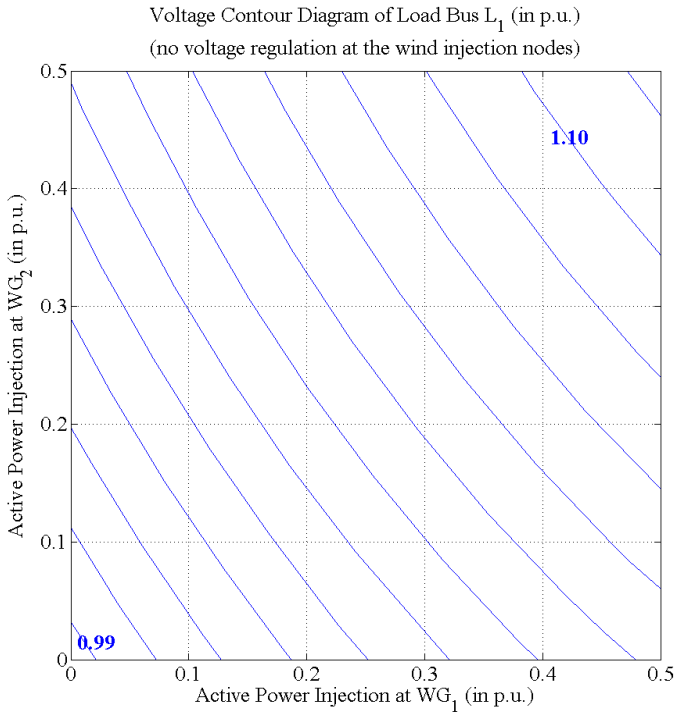

(b) Region of Interest

Figure 24: Contour diagrams of voltage magnitude at load bus L_1 for varying active power injections at wind nodes (no voltage regulation).

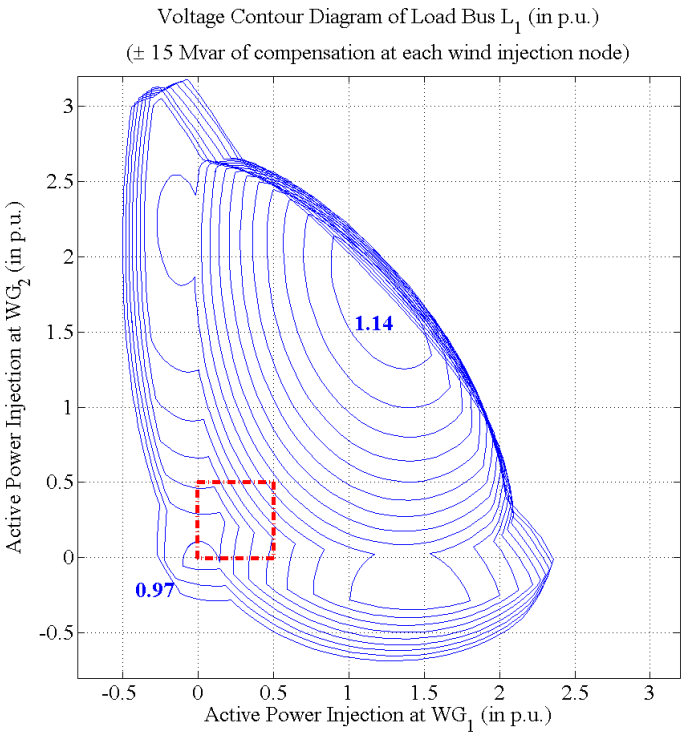

(a) Global

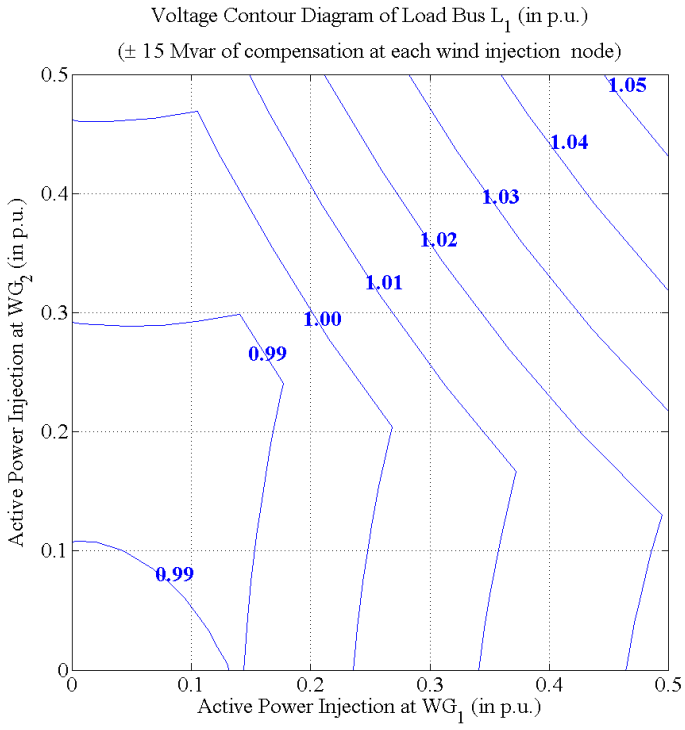

(b) Region of Interest

Figure 25: Contour diagrams of voltage magnitude at load bus L_1 for varying active power injections at wind nodes (±15 MVAr compensation).

Tap Step Sensitivities ($\frac{\text{step}}{\text{MW injection}}$)						
Operating Point	Injection Node	Transformer				
		T_1	T_2	T_3	T_4	T_5
No Wind Output	WG_1	-0.01	-0.03	-0.07	-0.09	0.00
	WG_2	-0.01	-0.01	-0.07	-0.07	0.00
40% Wind Output	WG_1	0.01	-0.01	-0.02	-0.03	0.01
	WG_2	0.01	0.00	-0.02	-0.02	0.02
80% Wind Output	WG_1	0.02	0.00	0.00	-0.01	0.03
	WG_2	0.02	0.00	0.00	0.00	0.03

Table 1: Tap step sensitivities for the transformers highlighted in Figure 23. No reactive compensation at wind-injection nodes.

Tap Step Sensitivities ($\frac{\text{step}}{\text{MW injection}}$)						
Operating Point	Injection Node	Transformer				
		T_1	T_2	T_3	T_4	T_5
No Wind Output	WG_1	0.04	0.04	0.10	0.11	0.07
	WG_2	0.05	0.04	0.14	0.09	0.06
40% Wind Output	WG_1	0.04	0.04	0.09	0.05	0.05
	WG_2	0.08	0.07	0.20	0.18	0.14
80% Wind Output	WG_1	0.03	0.01	0.02	0.03	0.05
	WG_2	0.03	0.01	0.02	0.03	0.06

Table 2: Tap step sensitivities for the transformers highlighted in Figure 23. Compensation of ± 15 MVAr at each wind-injection node.

where transformer taps are adjusted only in response to changes in the system load, must be compared with cases where variable wind is added, with and without local reactive compensation.

4.4 Wind and Tap Change Operation Simulation

The previous section established a relationship between voltage regulation of wind-injection nodes and sensitivity of the tap positions of the transformers that connect the sub-transmission and transmission systems. This will be explored further via simulation of the tap change operation of the five transformers in the system of interest.

The simulation is based on power flow code developed in Matlab and verified with commercial power flow programs. The simulation models tap position as a discrete variable. The power flow is executed every minute with updated load (P, Q) information for all buses in the network, and with minute-by-minute wind generation data. If the voltage of the bus that is regulated by a tap-changing transformer moves outside the deadband $(-\frac{1}{120}, +\frac{1}{120})$ p.u., centered on the voltage set-point, for two consecutive power flow executions (i.e. more than one minute) then the tap is adjusted accordingly (increased or decreased by a single step) to bring the voltage magnitude within the deadband. This reflects actual tap-changing operation, where the regulated voltage is allowed to deviate from the set-point by a certain margin for a certain period of time (typically one minute or up to several minutes depending on the setting of the transformer) before the tap-change operation is triggered. This mechanism is

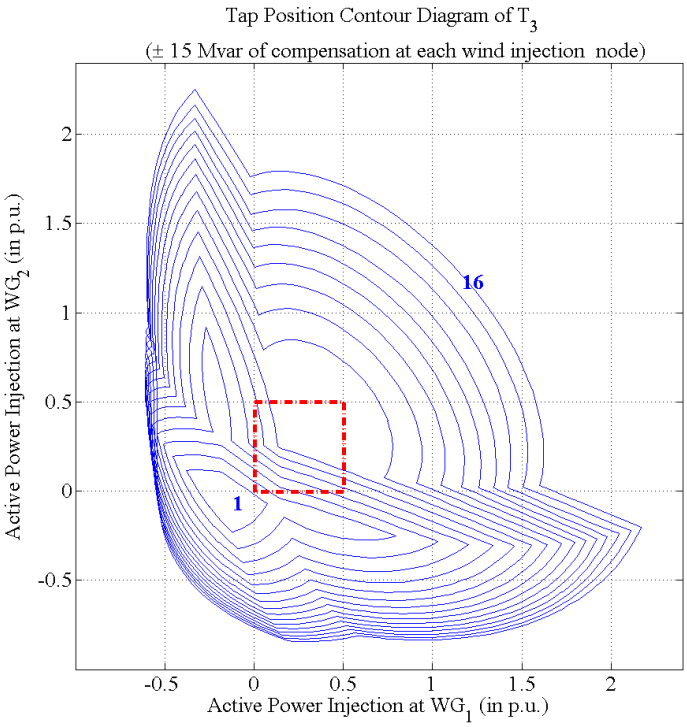

(a) Global

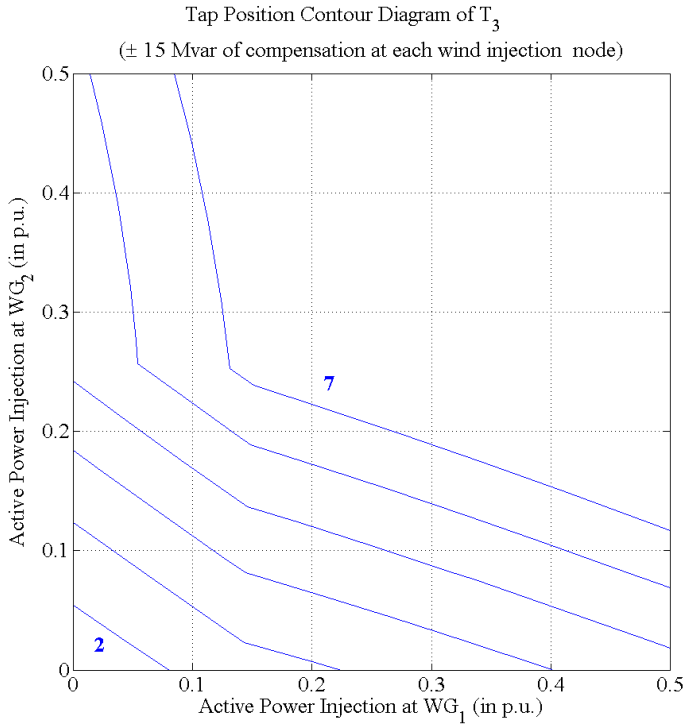

(b) Region of Interest

Figure 26: Contour diagram of T_3 tap position for varying active power injections at wind nodes (±15 MVAr compensation).

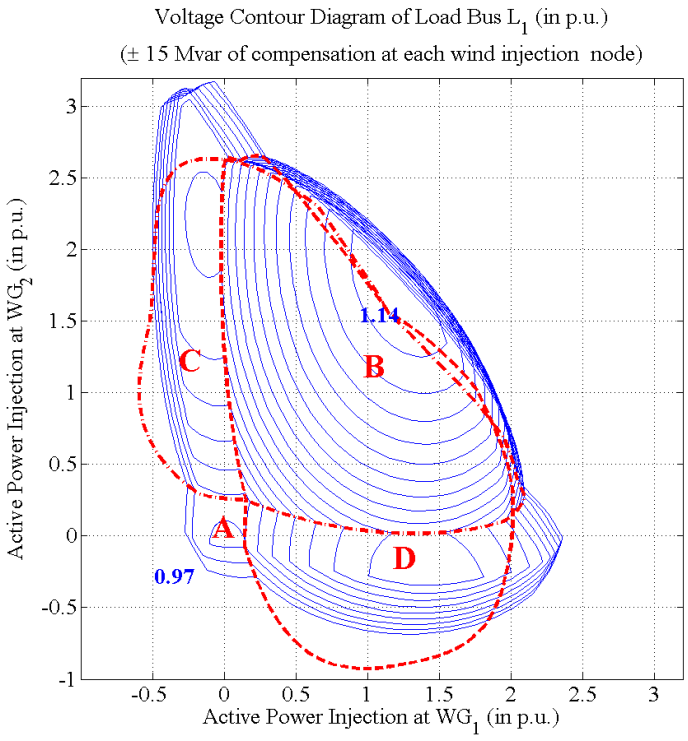

(a) Global

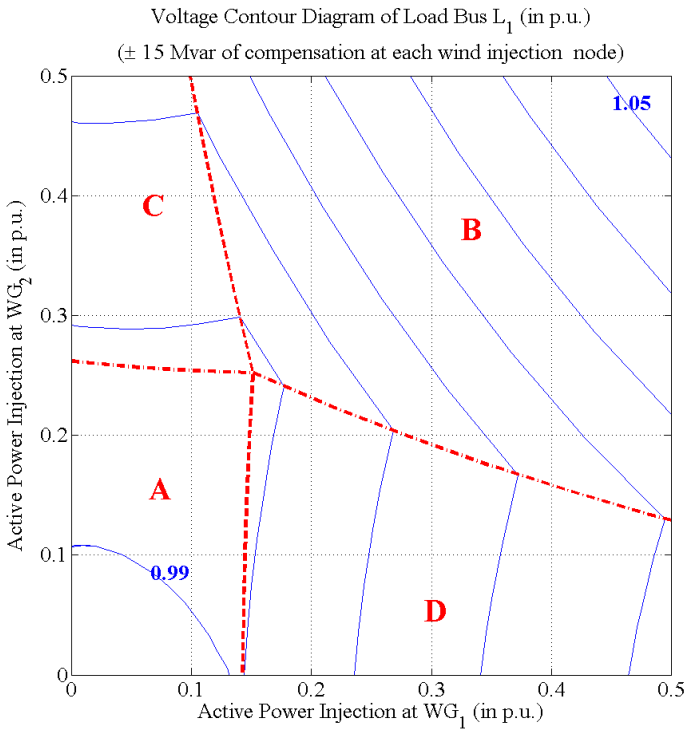

(b) Region of Interest

Figure 27: Demarcation of the L_1 voltage magnitude contour diagram into the four regions determined by reactive compensation limits.

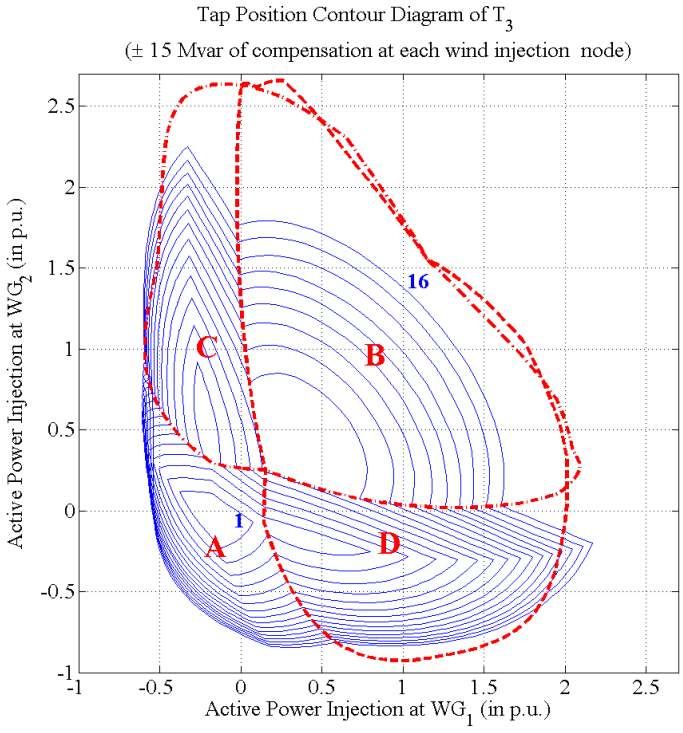

(a) Global

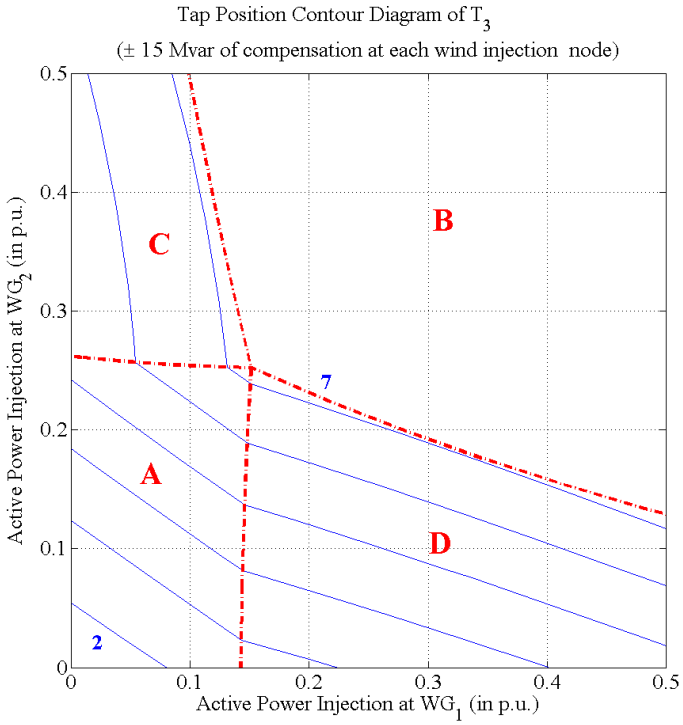

(b) Region of Interest

Figure 28: Demarcation of the T_3 tap position contour diagram into the four regions determined by reactive compensation limits.

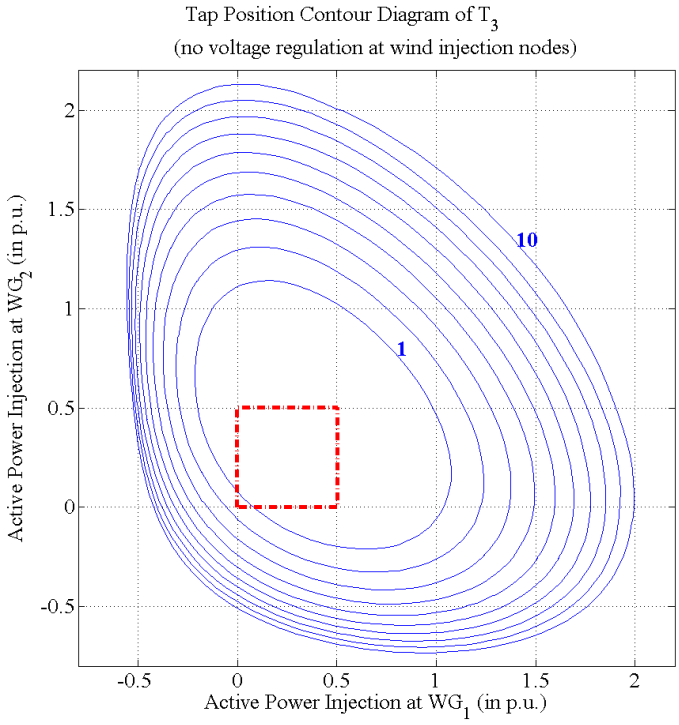

Figure 29: Contour diagram of T_3 tap position for varying active power injections at wind nodes (no voltage regulation).

designed to prevent small disturbances from triggering unnecessary tap-change operations.

The cases considered in the simulation study are as follows:

1. No Wind Injection.
2. Wind Injection at WG_1 (50 MW, $\pm$15 MVAr compensation).
3. Wind Injection at WG_2 (50 MW, $\pm$15 MVAr compensation).
4. Wind Injection at WG_1 and WG_2 (each 50 MW, no reactive compensation).
5. Wind Injection at WG_1 and WG_2 (each 50 MW, $\pm$15 MVAr compensation).

The simulations used load data for the south-east Michigan grid, and wind generation data from two wind-farms in Michigan, all with one minute resolution. Table 3 shows the number of tap changes per month for the five cases. It can be seen that wind injection in general increases tap change operation. However this increase is significant when both wind-farms WG_1 and WG_2 have local reactive compensation (voltage regulation).

Deeper insights can be obtained by considering the trend in the number of monthly tap change operations as the reactive compensation capacity at wind-injection nodes increases. This is shown in Figure 30. As the reactive compensation increases, the number of monthly tap operations initially remains relatively constant before starting to increase significantly around $\pm$10 MVAr. At that point the sub-transmission network begins to draw large amounts of reactive power from the 120 kV transmission system. Before the voltage regulating devices reach their inductive limits (as wind injection increases), more and more reactive power is

Number of Monthly Tap Changes					
Simulation Cases	Transformer				
	T_1	T_2	T_3	T_4	T_5
No Wind	140	23	98	85	173
WG_1 -/+15 Mvar	140	30	116	107	208
WG_2 -/+15 Mvar	142	44	154	102	230
WG_1 and WG_2 no compensation	142	28	134	113	176
WG_1 and WG_2 each -/+15 Mvar	213	105	511	456	442

Table 3: Number of monthly tap change operations for the transformers highlighted in Figure 23.

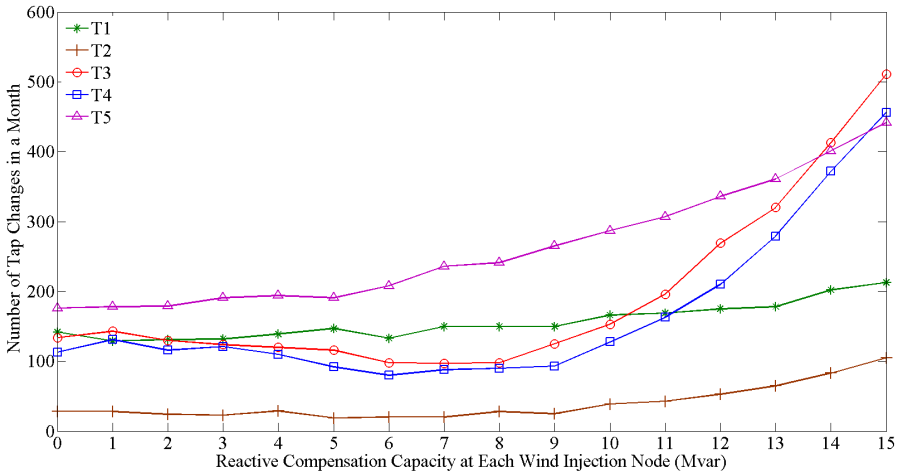

Figure 30: Number of monthly tap-change operations for each transformer, for varying reactive compensation capacity at wind-injection nodes.

drawn from the transmission system. This increase in reactive power flow causes the voltage on the primary side of the tap-changing transformers to drop, so the transformers respond by raising taps. Figure 31 illustrates the impact of greater reactive compensation on the transmission system voltage. For higher wind-power production, tighter voltage regulation at wind-injection nodes and nearby load buses comes at the cost of greater voltage deviations on the 120 kV transmission system.

4.5 Quadratic Optimization for Line Congestion

In order to minimize the cost of distribution networks, distribution line designs are usually closely tied to the load profile of the network and its growth projections. The addition of substantial wind power to such networks is, therefore, likely to cause overloading of line segments.

In a meshed network with multiple points of connection to the transmission system, as in Figure 23, varying wind generation patterns may cause line flows to vary in ways that are not always obvious. Consequently, line segments that are not even necessarily near wind-injection nodes may be driven to their limits as wind generation changes. On the other

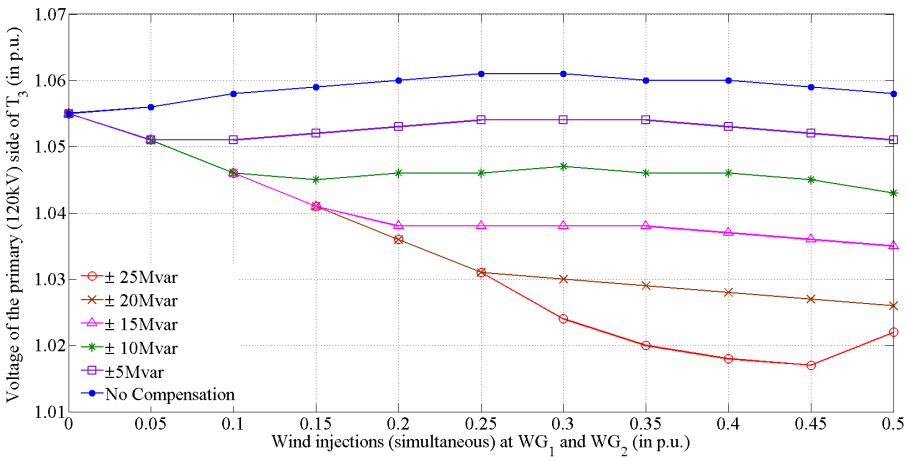

Figure 31: Voltage drop on the primary (120 kV) side of transformer T_3 for varying wind injection and different reactive compensation capacities.

hand, maximum generation at all wind-farms may not cause any congestion. It is therefore challenging to discover potential line overload vulnerabilities using conventional power-flow methods. To circumvent this difficulty, it would be useful to know the smallest change in the wind generation pattern that would cause any line segment to encounter its limit. This would immediately identify the most vulnerable line, as well as the most troublesome generation pattern.

Two optimization methods have been proposed for determining that information for any given operating point. Both are based on a convex quadratic optimization formulation, with the first using a DC power-flow approximation, and the second using AC sensitivities. The first of these methods shares some similarities with the instanton formulation developed in [57]. The DC method is more efficient computationally whereas the AC sensitivity-based method is more accurate. The AC approach may, however, require multiple iterations to achieve convergence, with each iteration solving a power flow and computing sensitivities. The AC formulation also does not provide any guarantee of a globally optimal solution, though based on experience, this does not seem to be an issue. Both methods take into account correlation between wind at different nodes.

4.5.1 DC power flow approximation

At the core of the DC quadratic optimization is the DC power flow. The usefulness of this optimization approach therefore depends on how accurately the DC power flow approximates actual line flows. It has been argued that the DC power flow may yield inaccurate approximations for networks where resistance is non-negligible ($\frac{X}{R} < 4$) [58, 59]. However, it was found for the power system of Figure 23, where $\frac{X}{R} \approx 1$, that the DC power flow approximation is quite accurate. Table 4 compares the DC approximation with the accurate AC power flow for the lines highlighted in green in Figure 23. The values in the table are given as a percentage of the line rating, and correspond to the case where each of the wind-farms in Figure 23 is producing 30 MW.

Line	DC Flow (%)	AC Flow (%)
1	66	55
2	45	43
3	82	84
4	107	95
5	114	90

Table 4: DC approximation of actual line flows, for lines highlighted in green in Figure 23.

4.5.2 DC quadratic optimization

Let the power generated at m wind-farms be described by the vector $\rho \in \mathbb{R}^m$. The wind-power generation pattern ρ that is closest (in a weighted 2-norm sense) to base-case generation ρ_0, and that causes line i to encounter its flow limit ℓ_i, is given by the DC quadratic optimization problem,

$$\bar{\rho}_i = \underset{\rho}{\operatorname{argmin}} \ \frac{1}{2}(\rho - \rho_0)^\top W(\rho - \rho_0) \tag{74}$$

subject to

$$\begin{bmatrix} A_\rho \\ A_b \end{bmatrix} \theta - \begin{bmatrix} \rho \\ b \end{bmatrix} = 0 \tag{75}$$

$$s_i^\top \theta - \ell_i = 0 \tag{76}$$

$$0 \leq \rho \leq \rho_{max} \tag{77}$$

where W is a symmetric, positive definite weighting matrix that captures the correlation between generation at the m wind-farms. For an n-bus network, bus phase angles are given by $\theta \in \mathbb{R}^{n-1}$, and non-wind power injections/loads by $b \in \mathbb{R}^{n-1-m}$. The admittance matrix $\begin{bmatrix} A_\rho \\ A_b \end{bmatrix}$ establishes a linear mapping between phase angles and power injections. Equation (76) forces the flow on a single chosen line i to equal its limit value, given by the scalar ℓ_i.

The Lagrangian [60] for this problem is given by,

$$\mathcal{L}(\rho, \theta, \lambda_\rho, \lambda_b, \gamma) = \frac{1}{2}(\rho - \rho_0)^\top W(\rho - \rho_0) + \lambda_\rho^\top (A_\rho \theta - \rho) + \lambda_b^\top (A_b \theta - b) + \gamma(s_i^\top \theta - \ell_i) \tag{78}$$

with the Karush-Kuhn-Tucker conditions [60] yielding the set of linear equations,

$$\frac{\partial \mathcal{L}}{\partial \rho} = (\rho - \rho_0)^\top W - \lambda_\rho^\top \qquad = 0 \tag{79}$$

$$\frac{\partial \mathcal{L}}{\partial \theta} = \begin{bmatrix} \lambda_\rho^\top & \lambda_b^\top \end{bmatrix} \begin{bmatrix} A_\rho \\ A_b \end{bmatrix} + \gamma s^\top = 0 \tag{80}$$

$$\frac{\partial \mathcal{L}}{\partial \lambda_\rho} = A_\rho \theta - \rho \qquad = 0 \tag{81}$$

$$\frac{\partial \mathcal{L}}{\partial \lambda_b} = A_b \theta - b \qquad = 0 \tag{82}$$

$$\frac{\partial \mathcal{L}}{\partial \gamma} = s_i^\top \theta - \ell_i \qquad = 0 \tag{83}$$

which can be expressed in matrix form as,

$$\begin{bmatrix} W & 0 & -I & 0 & 0 \\ 0 & 0 & A_\rho^\top & A_b^\top & s_i \\ -I & A_\rho & 0 & 0 & 0 \\ 0 & A_b & 0 & 0 & 0 \\ 0 & s_i^\top & 0 & 0 & 0 \end{bmatrix} \begin{bmatrix} \rho \\ \theta \\ \lambda_\rho \\ \lambda_b \\ \gamma \end{bmatrix} = \begin{bmatrix} W\rho_0 \\ 0 \\ 0 \\ b \\ \ell_i \end{bmatrix}. \tag{84}$$

This problem can be efficiently solved for large systems using standard sparse linear solvers. Note that the base-case generation ρ_0 appears only in the right hand side of (84). Therefore a range of base-case conditions can be evaluated efficiently through forward and backward substitution.

Because (84) considers only one line limit at a time, determining the most restrictive case from a set of candidate lines requires repeated solutions, with different line parameters (s_i, ℓ_i) for each case. The modifications required in (84) for each new case are minimal though, allowing efficient partial refactorization techniques [61] to be used to reduce the computational burden. Collecting the minima for all the candidate lines into the set $P = \{\bar{\rho}_1, \bar{\rho}_2, \dots\}$, the most restrictive case is given by,

$$\rho^* = \underset{\rho \in P}{\operatorname{argmin}} \ \frac{1}{2}(\rho - \rho_0)^\top W(\rho - \rho_0). \tag{85}$$

The network presented in Figure 23 provides a realistic test case for illustrating the DC optimization. The three wind-farms WG_1, WG_2 and WG_3 have the potential to overload the five feeders that are labelled and highlighted in green in the network diagram. For this initial case, it was assumed the outputs of the wind-farms were not correlated, so the weighting matrix W was set to the identity matrix. Table 5 presents the minimal wind generation that will drive each line to its limit. These results were obtained for $\rho_0 = 0$, as absolute generation levels were of interest, rather than changes from pre-existing loading conditions.

The insights provided by the results are helpful in understanding the influence of generation on feeder loadings. Line 1, for example, reaches its maximum loading when the flow is towards the south from WG_1, in the general direction of WG_2 and WG_3. When the other wind-farms generate, they produce a counter-flow on line 1, allowing WG_1 to further increase its output. Hence line 1 in most vulnerable to overload when WG_2 and WG_3 are out of service. Similarly, line 2 reaches its limit when flow is towards the west, from WG_2 in the direction of WG_1 and WG_3. In this case, generation at WG_1 and WG_3 will produce counter-flows on line 2, so this line is most vulnerable to overloading when those generators are not producing power. In the other cases, all generators contribute to line overloading, though typically the generator that is electrically closest has the greatest influence.

The value of the DC optimization can be further illustrated by considering vulnerability of lines when the wind-farms are operating at various different output levels. Table 6 lists operating points obtained from all combinations of low (10 MW) and high (30 MW) wind generation. Each case identifies the line that would reach its limit first as wind generation was increased, along with the corresponding change in wind-power production $\Delta\rho$. The effect of correlation between wind-farms was explored by first assuming no correlation, so W in (74) was simply the identity matrix. Secondly, it was assumed the three wind-farms tended to increase/decrease output in unison. In this latter case, the desired correlation matrix W was obtained by shaping the axes of the ellipsoids given by level-sets of the cost function

Line	WG_1	WG_2	WG_3
1	37	0	0
2	0	27	0
3	19	46	18
4	31	23	22
5	13	10	36

Table 5: Minimal wind injection needed to cause line congestion.

No.	Operating point			Congested line / $\Delta\rho$	
	WG_1	WG_2	WG_3	No Correlation	Correlation
1[a]	30	30	30	–	–
2	30	30	10	4 / [5,3,3]	4 / [4,4,4]
3	30	10	30	5 / [0,0,2]	5 / [1,1,1]
4	10	30	30	5 / [1,1,1]	5 / [1,1,1]
5	30	10	10	1 / [9 -1 -1]	1 / [10,4,4]
6	10	30	10	2 / [-3,5,-3]	2 / [-4,4,-4]
7	10	10	30	5 / [2,2,6]	5 / [4,4,5]
8	10	10	10	2 / [-10,17,-10]	5 / [14,13,19]

[a] Lines 4 and 5 are already congested according to the DC power flow approximation.

Table 6: Most vulnerable lines at each operating points, DC optimization.

(74). The axis in the direction $[1\ 1\ 1]^\top$ was scaled by a factor of 4 relative to the axes in the orthogonal directions. This scaling is illustrated in Figure 32, which shows a 2-dimensional projection of the level-sets. The resulting correlation matrix was

$$W = \begin{bmatrix} 3 & -1 & -1 \\ -1 & 3 & -1 \\ -1 & -1 & 3 \end{bmatrix}. \tag{86}$$

The results of Table 6 again reveal interesting trends in the relationships between generation patterns and line overloads. It can be seen that whenever WG_3 is heavily loaded, line 5 is the first to become congested. This is consistent with the findings of Table 5. Line 1 becomes limiting when WG_1 is heavily loaded, and the other wind-farms are not, which is again consistent with Table 5. There is a similar connection between WG_2 and line 2.

The eighth case is interesting in that correlation between wind-farms clearly affects the outcome. With no correlation, the most vulnerable loading direction $\Delta\rho = [-10\ 17\ -10]^\top$ has WG_2 increasing its output, while WG_1 and WG_3 reduce theirs. This would be unlikely if the outputs of all three wind-farms tended to change in unison. With correlation taken into account, the optimization has identified the more likely scenario of $\Delta\rho = [14\ 13\ 19]^\top$, where all wind-farms undergo a similar change.

4.5.3 AC sensitivity-based quadratic optimization

The DC quadratic optimization of (85) is guaranteed to give the globally optimal solution for the approximate DC system [60]. However, because of the approximation inherent in the

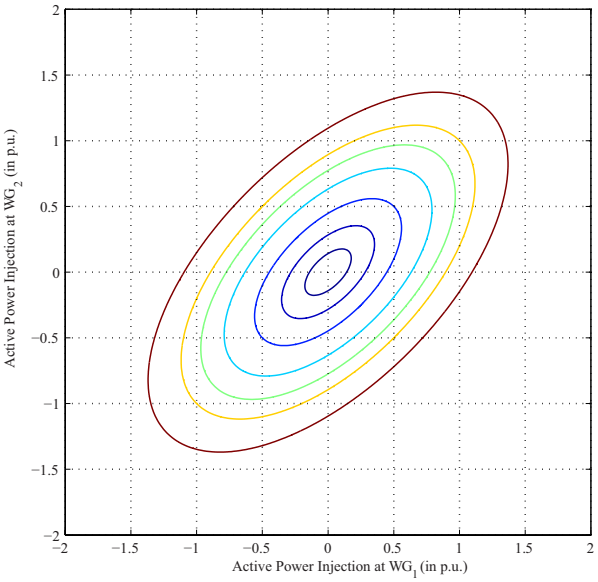

Figure 32: Ellipsoids generated by correlation matrix (86).

DC formulation, there is no guarantee that the line limits discovered are in fact the most restrictive. The AC sensitivity-based quadratic optimization provides increased accuracy over the DC method, though at an increased computational cost, and with no guarantee of achieving global optimality.

The magnitude of the current flow over a line between two nodes i and k can be written as the function,

$$I_{ik} = I_{ik}(\theta_i, \theta_k, V_i, V_k). \tag{87}$$

Linearizing gives

$$\Delta I_{ik} = \begin{bmatrix} \frac{\partial I_{ik}}{\partial \theta_i} & \frac{\partial I_{ik}}{\partial \theta_k} & \frac{\partial I_{ik}}{\partial V_i} & \frac{\partial I_{ik}}{\partial V_k} \end{bmatrix} \begin{bmatrix} \Delta\theta_i \\ \Delta\theta_k \\ \Delta V_i \\ \Delta V_k \end{bmatrix} \tag{88}$$

where the partial derivatives are evaluated at the operating point. Also, linearizing the power flow equations, as in (69), and inverting provides an approximate linear relationship between perturbations in power injection ΔP and ΔQ, and the corresponding perturbations in the state variables $\Delta\theta$ and $\Delta\mathcal{V}$. Assuming all perturbations in power injections are zero except for $\Delta\rho$ at wind-farms, perturbations in the states associated with nodes i and k are given by,

$$\begin{bmatrix} \Delta\theta_i \\ \Delta\theta_k \\ \Delta V_i \\ \Delta V_k \end{bmatrix} = \begin{bmatrix} S_{\theta[i,\rho]} \\ S_{\theta[k,\rho]} \\ S_{V[i,\rho]} \\ S_{V[k,\rho]} \end{bmatrix} \begin{bmatrix} \Delta\rho_1 \\ \vdots \\ \Delta\rho_m \end{bmatrix} \tag{89}$$

where S_V and S_θ follow from (71) and (72) respectively, and subscript $[i, \rho]$ refers to the i-th row and the subset of columns that correspond to ρ. Combining (88) and (89) allows the change in line current ΔI_{ik} to be related directly to changes in wind generation $\Delta\rho$ through,

$$\Delta I_{ik} = S_{I\rho}\Delta\rho. \tag{90}$$

If the line current limit of I_{ik}^{lim} and operating point value I_{ik}^{0} are sufficiently close, the linearization (90) can be used to establish a first-order approximation to the minimum change in wind power that would force the line to its limit. The resulting formulation is,

$$\Delta\bar{\rho}_{ik} = \underset{\Delta\rho}{\operatorname{argmin}} \ \frac{1}{2}\Delta\rho^{\top} W \Delta\rho \tag{91}$$

subject to

$$I_{ik}^{lim} - I_{ik}^{0} = \Delta I_{ik} = S_{I\rho}\Delta\rho. \tag{92}$$

The Lagrangian for this problem can be written as,

$$\mathcal{L}(\Delta\rho, \lambda) = \frac{1}{2}\Delta\rho^{\top} W \Delta\rho + \lambda\big(S_{I\rho}\Delta\rho - \Delta I_{ik}\big) \tag{93}$$

with the Karush-Kuhn-Tucker conditions yielding,

$$\frac{\partial\mathcal{L}}{\partial\Delta\rho} = \Delta\rho^{\top} W + \lambda S_{I\rho} = 0 \tag{94}$$

$$\frac{\partial\mathcal{L}}{\partial\lambda} = S_{I\rho}\Delta\rho - \Delta I_{ik} \ = 0 \tag{95}$$

or more compactly,

$$\begin{bmatrix} W & S_{I\rho}^{\top} \\ S_{I\rho} & 0 \end{bmatrix} \begin{bmatrix} \Delta\rho \\ \lambda \end{bmatrix} = \begin{bmatrix} 0 \\ \Delta I_{ik} \end{bmatrix}. \tag{96}$$

Solving (96) is straightforward, and yields an estimate $\Delta\bar{\rho}_{ik}$ of the change in wind-power output that is most likely to drive line i-k to its limit. That estimate can be used in an iterative scheme:

1. Update wind-power production $\rho + \Delta\bar{\rho}_{ik}$,
2. Solve the AC power flow for the new operating point,
3. Calculate new sensitivities, and
4. Repeat the optimization.

This process often converges reliably within 1-2 iterations. This iterative solution process is then repeated for each line in a specified set of candidate lines. The line that is most restrictive, in the W-norm sense of (85), establishes the most vulnerable loading direction for the wind-farms.

Table 7 lists the lines identified as the most vulnerable for the same set of operating points as in Table 6. Again, the influence of correlation between wind-farms has been considered.

4.5.4 Comparison of the results

There is generally strong qualitative agreement between the DC and AC optimization results presented in Tables 6 and 7 respectively. This is particularly so for the operating points that are more heavily loaded. In cases where the two methods identified different lines, the DC results were investigated further. It was found that the difference in cost (85) between the two most vulnerable lines was small. In such cases, typically the second ranked line matched the line selected by the AC optimization.

Computationally, the efficiency of the DC optimization provides a significant advantage when analyzing systems with large numbers of wind-farms and numerous lines that are susceptible to overloading.

No.	Operating point			Congested line / $\Delta\rho$	
	WG_1	WG_2	WG_3	No Correlation	Correlation
1	30	30	30	4 / [1,1,1]	4 / [1,1,1]
2	30	30	10	4 / [9,6,6]	4 / [8,7,7]
3	30	10	30	5 / [2,2,8]	5 / [5,5,6]
4	10	30	30	5 / [3,2,9]	5 / [5,5,7]
5	30	10	10	1 / [14,-5,-6]	4 / [14,13,13]
6	10	30	10	2 / [-8,3,-8]	3 / [12,15,12]
7	10	10	30	5 / [4,3,13]	5 / [8,8,11]
8	10	10	10	5 / [10,7,31]	4 / [22,21,20]

Table 7: Most vulnerable lines at each operating points, AC optimization.

4.6 Conclusions

The analysis tools presented in this chapter are well suited to assessing the impact of wind variability on bus voltages, voltage regulating transformers and line flows. These tools provide valuable insights into the effects of wind generation on sub-transmission and distribution networks. Because of the relative weakness of these networks, wind variability can induce unacceptable voltage excursions, excessive transformer tapping, and line overloads. The tools that have been presented not only help identify vulnerabilities within networks, but can also offer insights into ways to retune parameters to mitigate the impacts of wind variability. This will help pave the way for higher penetration of wind and other intermittent renewable resources into weak networks.

Although voltage regulation at the point of wind interconnection is indispensable, the analysis presented in this chapter suggests that it has a detrimental effect on tap-changer operation for the transformers that connect the sub-transmission network (40 kV) to the transmission system (120 kV). Wind-farm voltage regulation tends to increase the sensitivity of tap position to wind-power variations, and significantly increases the number of tap change operations. Consequently, the life of these expensive assets will be decreased, hindering the development of wind power in weak grids.

The simulation results presented in this chapter indicate that the tap positions of the 120/40 kV transformers tend to remain relatively constant when the voltage at wind-injection nodes in not regulated. On the other hand, lack of voltage regulation at wind-farms leads to unacceptable voltage fluctuations within the sub-transmission network. This highlights the importance of optimizing the size of reactive compensation to balance voltage fluctuations and tap changing.

Appendices

A Switched equations for WT3E

In the following set of switched equations, (97) implements the rate limits associated with the P_{ord} block, establishing the rate-limited signal $P_{ord,rtlm}$ that drives P_{ord} in (3). Equations (98) and (99) implement the P_{max} and P_{min} non-windup limits respectively. Consider the P_{max} limit described by (98). While $P_{ord} \leq P_{max}$, the trigger variable $y_{mx} \geq 0$, so the switch $y_{mx,sw} = 1$. This ensures the integrator (3) is not blocked. On the other hand, if system conditions sought to drive P_{ord} beyond P_{max}, then y_{mx} would immediately change sign, triggering $y_{mx,sw}$ to switch to 0. That would force the right hand side of integrator (3) to zero, ensuring P_{ord} was frozen at its P_{max} limit. While $P_{ord,rtlm}$ remained positive, seeking to drive P_{ord} harder onto the limit, the trigger variable $y_{mx} < 0$. As soon as $P_{ord,rtlm}$ changed sign though, allowing P_{ord} to come off its limit, y_{mx} would also change sign, and $y_{mx,sw}$ would switch to 1, thus re-enabling the integrator (3). Similar logic applies in (99) for the P_{min} limit.

Equation (100) enforces the rules specified in (i) and (ii) of Section 2.2.1 that link the blocking of the PI-integrator with the P_{ord} limit conditions. It does so through the use of switch variable y_{freeze} that is used to turn on/off the integrator (2).

$$
\left.\begin{array}{l}
\text{if } P_{ord,rate} > dP_{max}/dt \\
\quad P_{ord,rtlm} = dP_{max}/dt \\
\text{elseif } P_{ord,rate} < -dP_{max}/dt \\
\quad P_{ord,rtlm} = -dP_{max}/dt \\
\text{else} \\
\quad P_{ord,rtlm} = P_{ord,rate} \\
\text{endif}
\end{array}\right\} \tag{97}
$$

$$
\left.\begin{array}{l}
\text{if } y_{mx} \geq 0 \\
\quad y_{mx} = P_{max} - P_{ord} \\
\quad y_{mx,sw} = 1 \\
\text{else} \\
\quad y_{mx} = -P_{ord,rtlm} \\
\quad y_{mx,sw} = 0 \\
\text{endif}
\end{array}\right\} \tag{98}
$$

$$
\left.\begin{array}{l}
\text{if } y_{mn} \geq 0 \\
\quad y_{mn} = P_{ord} - P_{min} \\
\quad y_{mn,sw} = 1 \\
\text{else} \\
\quad y_{mn} = P_{ord,rtlm} \\
\quad y_{mn,sw} = 0 \\
\text{endif}
\end{array}\right\} \tag{99}
$$

$$
\left.
\begin{array}{l}
\text{if } y_{mx,sw} = 0 \text{ and } \omega - \omega_{ref} > 0 \\
\qquad y_{freeze} = 0 \\
\text{elseif } y_{mn,sw} = 0 \text{ and } \omega - \omega_{ref} < 0 \\
\qquad y_{freeze} = 0 \\
\text{else} \\
\qquad y_{freeze} = 1 \\
\text{endif}
\end{array}
\right\} \tag{100}
$$

B Switched equations for WT3P

In the following set of switched equations, (101) implements the rate limit associated with the θ block, establishing the rate-limited signal θ_{rtlm} that drives θ in (7). Equations (102) and (103) implement the PI_{max} and PI_{min} non-windup limits respectively, while (104) models the lower non-windup limit on the pitch compensation integrator. Equations (105) and (106) enforce the rules that link the blocking of the pitch-control and pitch-compensation integrators to the PI_{max}/PI_{min} non-windup limits.

$$
\left.
\begin{array}{l}
\text{if } \theta_{rate} > PI_{rate} \\
\qquad \theta_{rtlm} = PI_{rate} \\
\text{else} \\
\qquad \theta_{rtlm} = \theta_{rate} \\
\text{endif}
\end{array}
\right\} \tag{101}
$$

$$
\left.
\begin{array}{l}
\text{if } y_{mx} \geq 0 \\
\qquad y_{mx} = PI_{max} - \theta \\
\qquad y_{mx,sw} = 1 \\
\text{else} \\
\qquad y_{mx} = -\theta_{rtlm} \\
\qquad y_{mx,sw} = 0 \\
\text{endif}
\end{array}
\right\} \tag{102}
$$

$$
\left.
\begin{array}{l}
\text{if } y_{mn} \geq 0 \\
\qquad y_{mn} = \theta - PI_{min} \\
\qquad y_{mn,sw} = 1 \\
\text{else} \\
\qquad y_{mn} = \theta_{rtlm} \\
\qquad y_{mn,sw} = 0 \\
\text{endif}
\end{array}
\right\} \tag{103}
$$

$$
\left.
\begin{array}{l}
\text{if } y_{xc} \geq 0 \\
\qquad y_{xc} = x_c - x_{c,lim} \\
\qquad y_{sw} = 1 \\
\text{else} \\
\qquad y_{xc} = P_{ord} - P_{set} \\
\qquad y_{sw} = 0 \\
\text{endif}
\end{array}
\right\} \tag{104}
$$

$$
\left.
\begin{array}{l}
\text{if } y_{mx,sw} = 0 \text{ and } \omega - \omega_{ref} > 0 \\
\qquad y_{fr,1} = 0 \\
\text{elseif } y_{mn,sw} = 0 \text{ and } \omega - \omega_{ref} < 0 \\
\qquad y_{fr,1} = 0 \\
\text{else} \\
\qquad y_{fr,1} = 1 \\
\text{endif}
\end{array}
\right\} \tag{105}
$$

$$
\left.
\begin{array}{l}
\text{if } y_{mx,sw} = 0 \text{ and } P_{ord} - P_{set} > 0 \\
\qquad y_{fr,2} = 0 \\
\text{elseif } y_{mn,sw} = 0 \text{ and } P_{ord} - P_{set} < 0 \\
\qquad y_{fr,2} = 0 \\
\text{else} \\
\qquad y_{fr,2} = 1 \\
\text{endif}
\end{array}
\right\} \tag{106}
$$

C WECC default parameter values

The test system is given in Figure 33. Parameter values are given in Tables 8 to 14. The wind-generator output is 100 MW = 1.0 pu. A 10 MVAr capacitor is connected at bus 3, but no shunt is connected at bus 5.

A three-phase fault is applied at bus 2 at 1 sec. It is cleared at 1.15 sec by disconnecting one of the 230 kV transmission lines.

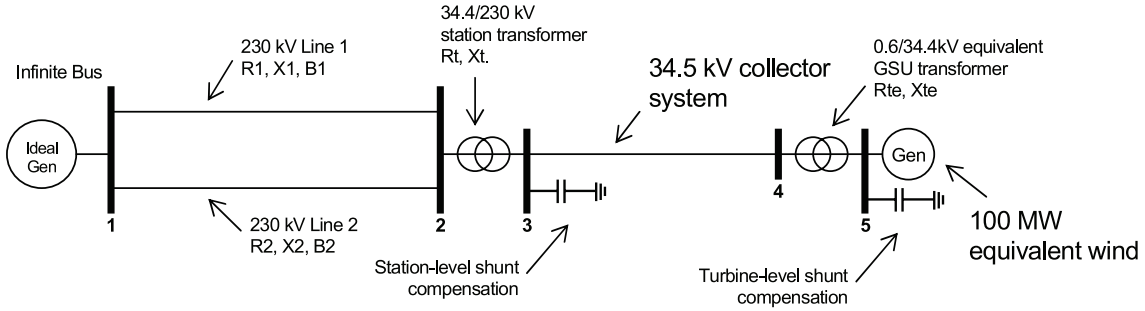

Figure 33: Standard test system for evaluating WTG dynamic performance.

$R_1 = R_2$	$X_1 = X_2$	$B_1 = B_2$	R_t	X_t
0.025	0.250	0.05	0.0	0.1
R_e	X_e	B_e	R_{te}	X_{te}
0.015	0.025	0.01	0.0	0.05

Table 8: Impedance values for the test system of Figure 33.

X_{eq}	K_{pll}	K_{ipll}	P_{llmax}
0.8	30	1	0.1

Table 9: Parameter values for WT3G.

varflg	vltflg	V_{ref}	K_{qi}	V_{max}	V_{min}
0	0	1	0.1	1.1	0.9

Table 10: Parameter values for WT3E reactive power control.

K_{ptrq}	K_{itrq}	T_{pc}	P_{min}	P_{max}	I_{pmax}	dP_{max}/dt	T_{sp}
3	0.6	0.05	0.04	1.12	1.1	0.45	5

Table 11: Parameter values for WT3E active power (torque) control.

ω_{pmin}	ω_{p20}	ω_{p40}	ω_{p60}	$P_{\omega p100}$	ω_{p100}
0.69	0.78	0.98	1.12	0.74	1.2

Table 12: Parameter values for speed-power curve $f(P_{gen})$.

K_{aero}	θ_0	P_{m0}	H	D
0.007	0	1	4.94	0

Table 13: Parameter values for WT3T single-shaft model.

K_{pp}	K_{ip}	K_{pc}	K_{ic}	T_{PI}	PI_{max}	PI_{min}	PI_{rate}	P_{set}
150	25	3	30	0.3	27	0	10	1

Table 14: Parameter values for WT3P.

References

[1] T. Ackermann (Editor), *Wind Power in Power Systems.* England: John Wiley and Sons, 2005.

[2] E. Muljadi, C. Butterfield, B. Parsons, and A. Ellis, "Effect of variable speed wind turbine generator on stability of a weak grid," *IEEE Transactions on Energy Conversion*, vol. 22, no. 1, pp. 29–36, March 2007.

[3] D. Gautam, V. Vittal, and T. Harbour, "Impact of increased penetration of DFIG-based wind turbine generators on transient and small signal stability of power systems," *IEEE Transactions on Power Systems*, vol. 24, no. 3, pp. 1426–1434, August 2009.

[4] M. Nunes, J. Lopes, H. Zurn, U. Bezerra, and R. Almeida, "Influence of the variable-speed wind generators in transient stability margin of the conventional generators integrated in electrical grids," *IEEE Transactions on Energy Conversion*, vol. 19, no. 4, pp. 692–701, December 2004.

[5] N. Ullah and T. Thiringer, "Effect of operational modes of a wind farm on the transient stability of nearby generators and on power oscillations: a Nordic grid study," *Wind Energy*, vol. 11, pp. 63–73, September 2007.

[6] D. Kosterev and D. Davies, "System model validation studies in WECC," in *Proceedings of the IEEE PES General Meeting*, Minneapolis, MN, July 2010.

[7] I. Hiskens and J. Alseddiqui, "Sensitivity, approximation and uncertainty in power system dynamic simulation," *IEEE Transactions on Power Systems*, vol. 21, no. 4, pp. 1808–1820, November 2006.

[8] J. Slootweg, S. de Haan, H. Polinder, and W. Kling, "General model for representing variable speed wind turbines in power system dynamics simulations," *IEEE Transactions on Power Systems*, vol. 18, no. 1, pp. 144–151, February 2003.

[9] J. Ekanayake, L. Holdsworth, X.-G. Wu, and N. Jenkins, "Dynamic modeling of doubly fed induction generator wind turbines," *IEEE Transactions on Power Systems*, vol. 18, no. 2, pp. 803–809, May 2003.

[10] Y. Lei, A. Mullane, G. Lightbody, and R. Yacamini, "Modeling of the wind turbine with a doubly fed induction generator for grid integration studies," *IEEE Transactions on Energy Conversion*, vol. 21, no. 1, pp. 257–264, March 2006.

[11] M. Kayikçi and J. Milanović, "Assessing transient response of DFIG-based wind plants - The influence of model simplifications and parameters," *IEEE Transactions on Power Systems*, vol. 23, no. 2, pp. 545–554, May 2008.

[12] J. Rose and I. Hiskens, "Estimating wind turbine parameters and quantifying their effects on dynamic behavior," in *Proceedings of the IEEE PES General Meeting*, Pittsburgh, PA, July 2008.

[13] K. Clark, N. Miller, and J. Sanchez-Gasca, "Modeling of GE wind turbine-generators for grid studies," Version 4.4, GE Energy, September 2009.

[14] E. Muljadi, C. Butterfield, J. Conto, and K. Donoho, "ERCOT's dynamic model of wind turbine generators," in *Proceedings of WindPower 2005*, Denver, CO, May 2005.

[15] "Generic type-3 wind turbine-generator model for grid studies," Version 1.1, WECC Wind Generator Modeling Group, September 2006.

[16] "WECC wind power plant dynamic modeling guide," WECC Renewable Energy Modeling Task Force, November 2010.

[17] Z. Lubosny, *Wind Turbine Operation in Electric Power Systems*. Springer, 2003.

[18] A. van der Schaft and H. Schumacher, *An Introduction to Hybrid Dynamical Systems*. London: Springer-Verlag, 2000.

[19] D. Liberzon, *Switching in Systems and Control*. Boston: Birkhauser, 2003.

[20] I. Hiskens, "Power system modeling for inverse problems," *IEEE Transactions on Circuits and Systems I: Regular Papers*, vol. 51, no. 3, pp. 539–551, March 2004.

[21] IEEE Std 421.5-2005, *IEEE Recommended Practice for Excitation System Models for Power System Stability Studies*. New York: Institute of Electrical and Electronics Engineers, Inc., 2005.

[22] A. Abate, A. D'Innocenzo, M. Di Benedetto, and S. Sastry, "Understanding deadlock and livelock behaviors in hybrid control systems," *Nonlinear Analysis: Hybrid Systems*, vol. 3, no. 2, pp. 150–162, May 2009.

[23] I. Hiskens and P. Sokolowski, "Systematic modeling and symbolically assisted simulation of power systems," *IEEE Transactions on Power Systems*, vol. 16, no. 2, pp. 229–234, May 2001.

[24] H. Khalil, *Nonlinear Systems*, 3rd ed. Upper Saddle River, NJ: Prentice Hall, 2001.

[25] I. Hiskens and D. Hill, "Energy functions, transient stability and voltage behaviour in power systems with nonlinear loads," *IEEE Transactions on Power Systems*, vol. 4, no. 4, pp. 1525–1533, November 1989.

[26] V. Venkatasubramanian, H. Schättler, and J. Zaborszky, "Dynamics of large constrained nonlinear systems - a taxonomy theory," *Proceedings of the IEEE*, vol. 83, no. 11, pp. 1530–1561, November 1995.

[27] A. Filippov, *Differential Equations with Discontinuous Righthand Sides*. The Netherlands: Kluwer Academic Publishers, 1988.

[28] V. Utkin, J. Guldner, and J. Shi, *Sliding Mode Control in Electro-Mechanical Systems*, 2nd ed. CRC Press, 2009.

[29] I. Hiskens, "Trajectory deadlock in power system models," in *Proceedings of the IEEE International Symposium on Circuits and Systems*, Rio de Janeiro, Brazil, May 2011, pp. 2721–2724.

[30] I. Hiskens and M. Pai, "Trajectory sensitivity analysis of hybrid systems," *IEEE Transactions on Circuits and Systems I: Fundamental Theory and Applications*, vol. 47, no. 2, pp. 204–220, February 2000.

[31] R. Cottle, J.-S. Pang, and R. Stone, *The Linear Complementarity Problem*. Boston, MA: Academic Press, 1992.

[32] A. van der Schaft and J. Schumacher, "Complementarity modeling of hybrid systems," *IEEE Transactions on Automatic Control*, vol. 43, no. 4, pp. 483–490, April 1998.

[33] E. Camm, M. Behnke, O. Bolado, M. Bollen, M. Bradt, C. Brooks, W. Dilling, M. Edds, W. Hejdak, D. Houseman, S. Klein, F. Li, J. Li, P. Maibach, T. Nicolai, J. Patino, S. V. Pasupulati, N. Samaan, S. Saylors, T. Siebert, T. Smith, M. Starke, and R. Walling, "Reactive power compensation for wind power plants," in *Proceedings of the IEEE PES General Meeting*, Calgary, Alberta, July 2009.

[34] ——, "Wind power plant substation and collector system redundancy, reliability, and economics," in *Proceedings of the IEEE PES General Meeting*, Calgary, Alberta, July 2009.

[35] ——, "Characteristics of wind turbine generators for wind power plants," in *Proceedings of the IEEE PES General Meeting*, Calgary, Alberta, July 2009.

[36] D. Bertsekas, *Dynamic Programming and Optimal Control Vol 1.* Athena Scientific, 2005.

[37] ——, *Dynamic Programming and Optimal Control Vol 2.* Athena Scientific, 2005.

[38] K. Brokish and J. Kirtley, "Pitfalls of modeling wind power using markov chains," in *Proceedings of the IEEE Power Systems Conference and Exposition*, Seattle, WA, March 2009.

[39] I. Erlich and H. Brakelmann, "Integration of wind power into the German high voltage transmission grid," in *Proceedings of the IEEE PES General Meeting*, Tampa, FL, July 2007.

[40] A. Tapia, G. Tapia, and J. Ostolaza, "Reactive power control of windfarms for voltage control applications," *Renewable Energy*, vol. 29, p. 377392, 2004.

[41] J. L. Rodriguez-Amenedo, S. Arnalte, and J. C. Burgos, "Automatic generation control of a wind farm with variable speed wind turbines," *IEEE Transaction on Energy Conversion*, vol. 17, no. 2, pp. 279–284, Jun. 2002.

[42] W. Kersting, *Distribution System Modeling and Analysis*, 3rd ed. CRC Press, 2012.

[43] P. Carvalho, P. Correia, and L. Ferreira, "Distributed reactive power generation control for voltage rise mitigation in distribution networks," *IEEE Transactions on Power Systems*, vol. 23, no. 2, pp. 766–772, May 2008.

[44] J. Peschon, D. Piercy, W. Tinney, and O. Tveit, "Sensitivity in power systems," *IEEE Transactions on Power Apparatus and Systems*, vol. PAS-87, no. 8, pp. 1687–1696, August 1968.

[45] M. Begovic and A. Phadke, "Control of voltage stability using sensitivity analysis," *IEEE Transactions on Power Systems*, vol. 7, no. 1, pp. 114–123, February 1992.

[46] F. Capitanescu and T. Van Cutsem, "Unified sensitivity analysis of unstable or low voltages caused by load increases or contingencies," *IEEE Transactions on Power Systems*, vol. 20, no. 1, pp. 321–329, February 2005.

[47] N. Flatabo, O. Fosso, R. Ognedal, and T. Carlsen, "A method for calculation of margins to voltage instability applied on the Norwegian system for maintaining required security level," *IEEE Transactions on Power Systems*, vol. 8, no. 3, pp. 920–928, August 1993.

[48] L. Soder, "Estimation of reduced electrical distribution losses depending on dispersed small scale energy production," in *Proceedings of 12th Power Systems Computation Conference*, vol. 2, Zurich, Switzerland, 1996, pp. 1229–1234.

[49] C. Garcia and W. Zangwill, *Pathways to Solutions, Fixed Points and Equilibria*. Englewood Cliffs, NJ: Prentice Hall, 1981.

[50] G. Price, "A generalized circle diagram approach for global analysis of transmission system performance," *IEEE Transactions on Power Apparatus and Systems*, vol. PAS-103, no. 10, pp. 2881–2890, October 1984.

[51] V. Ajjarapu and C. Christy, "The continuation power flow: a tool for steady state voltage stability analysis," *IEEE Transactions on Power Systems*, vol. 7, no. 1, pp. 416–423, February 1992.

[52] I. Hiskens and R. Davy, "Exploring the power flow solution space boundary," *IEEE Transactions on Power Systems*, vol. 16, no. 3, pp. 389–395, August 2001.

[53] J. Glover, M. Sarma, and T. Overbye, *Power System Analysis and Design*, 5th ed. CL-Engineering, 2012.

[54] D. Bernstein, *Matrix Mathematics: Theory, Facts and Formulas*, 2nd ed. Princeton University Press, 2009.

[55] R. Seydel, *Practical Bifurcation and Stability Analysis*, 2nd ed. New York: Springer-Verlag, 1994.

[56] C. Masters, "Voltage rise: the big issue when connecting embedded generation to long 11 kv overhead lines," *IEE Power Engineering Journal*, vol. 16, no. 1, pp. 5–12, February 2002.

[57] M. Chertkov, M. Stepanov, F. Pan, and R. Baldick, "Exact and efficient algorithm to discover extreme stochastic events in wind generation over transmission power grids," in *Proceedings of the 50th IEEE Conference on Decision and Control*, Orlando, FL, December 2011, pp. 2174–2180.

[58] K. Purchala, L. Meeus, D. V. Dommelen, and R. Belmans, "Usefulness of DC power flow for active power flow analysis," in *Proceedings of the IEEE PES General Meeting*, San Francisco, CA, July 2005.

[59] B. Stott, J. Jardim, and O. Alsac, "DC power flow revisited," *IEEE Transactions on Power Systems*, vol. 24, no. 3, pp. 1290–1300, August 2009.

[60] J. Nocedal and S. Wright, *Numerical Optimization*, 2nd ed. Springer, 2006.

[61] S. Chan and V. Brandwajn, "Partial matrix refactorization," *IEEE Transactions on Power Systems*, vol. 1, no. 1, pp. 193–199, February 1986.